

# Dynamics in Fip1 regulate eukaryotic mRNA 3' end processing

Ananthanarayanan Kumar,<sup>1,2</sup> Conny W.H. Yu,<sup>2</sup> Juan B. Rodríguez-Molina, Xiao-Han Li, Stefan M.V. Freund, and Lori A. Passmore

MRC Laboratory of Molecular Biology, Cambridge CB2 0QH, United Kingdom

**Cleavage and polyadenylation factor (CPF/CPSF) is a multiprotein complex essential for mRNA 3' end processing in eukaryotes. It contains an endonuclease that cleaves pre-mRNAs, and a polymerase that adds a poly(A) tail onto the cleaved 3' end. Several CPF subunits, including Fip1, contain intrinsically disordered regions (IDRs). IDRs within multiprotein complexes can be flexible, or can become ordered upon interaction with binding partners. Here, we show that yeast Fip1 anchors the poly(A) polymerase Pap1 onto CPF via an interaction with zinc finger 4 of another CPF subunit, Yth1. We also reconstitute a fully recombinant 850-kDa CPF. By incorporating selectively labeled Fip1 into recombinant CPF, we could study the dynamics of Fip1 within the megadalton complex using nuclear magnetic resonance (NMR) spectroscopy. This reveals that a Fip1 IDR that connects the Yth1- and Pap1-binding sites remains highly dynamic within CPF. Together, our data suggest that Fip1 dynamics within the 3' end processing machinery are required to coordinate cleavage and polyadenylation.**

[*Keywords:* CPF; CPSF; RNA-binding protein; dynamics; mRNA processing; polyadenylation]

Supplemental material is available for this article.

Received May 16, 2021; revised version accepted September 9, 2021.

Protein-coding genes in eukaryotes are transcribed by RNA polymerase II (Pol II) into precursor messenger RNAs (pre-mRNAs). Pre-mRNAs are modified by the addition of a 7-methylguanosine cap at the 5' end, splicing, and 3' end processing (Hocine et al. 2010). The 3' end of an mRNA is formed by a two-step reaction involving endonucleolytic cleavage at a specific site and the addition of a stretch of polyadenosines [a poly(A) tail] to the new free 3' hydroxyl (Zhao et al. 1999). Poly(A) tails are essential for export of mature mRNAs into the cytoplasm, for their subsequent translation into proteins, and in determining mRNA half-life. Defects in 3' end processing are associated with human diseases including cancer,  $\beta$ -thalassemia, and spinal muscular atrophy (Curinha et al. 2014). Understanding the mechanistic basis of 3' end processing and how cleavage and polyadenylation are coordinated with other mRNA processing steps is therefore of great importance.

Eukaryotic 3' end processing is carried out by a set of conserved multiprotein complexes that includes the cleavage and polyadenylation factor (CPF in yeast or CPSF in humans) and accessory cleavage factors (CF IA and CF IB in yeast or CF IIm, CF IIIm, and CstF in humans)

(Kumar et al. 2019). In yeast, CPF is comprised of three enzymatic modules: a five-subunit polymerase module containing the poly(A) polymerase Pap1, a three-subunit nuclease module containing the endonuclease Ysh1, and a six-subunit phosphatase module that includes two protein phosphatases (Glc7 and Swd2) that regulate transcription (Casañal et al. 2017). Most CPF subunits are conserved across all eukaryotes.

Insights into the molecular basis of polyadenylation have been obtained through structural and biochemical studies. For example, a crystal structure of Pap1 in complex with ATP, poly(A) RNA, and  $Mg^{2+}$  confirmed that a two-metal ion-dependent nucleotidyl transfer mechanism is used in poly(A) tail synthesis (Balbo and Bohm 2007). Together with kinetic studies, this structure provided a molecular basis for nucleotide specificity. Pap1 is assembled into the polymerase module along with Cft1, Pfs2, the zinc finger-containing protein Yth1, and the low-sequence-complexity protein Fip1 (Casañal et al. 2017). A similar mammalian polymerase module (mPSF) is sufficient for specific and efficient mRNA polyadenylation in vitro (Schönemann et al. 2014). Cryo-electron microscopy (cryoEM) structures of the polymerase modules from yeast and humans revealed an extensive network of interactions between Pfs2 and Cft1 (WDR33 and CPSF160 in humans), which function as a scaffold for assembly of the other subunits (Casañal et al. 2017;

<sup>1</sup>Present address: Department of Molecular, Cellular, and Developmental Biology, Yale University, New Haven, CT 06511, USA.

<sup>2</sup>These authors contributed equally to this work.

Corresponding authors: passmore@mrc-lmb.cam.ac.uk, smvf@mrc-lmb.cam.ac.uk

Article published online ahead of print. Article and publication date are online at <http://www.genesdev.org/cgi/doi/10.1101/gad.348671.121>. Freely available online through the *Genes & Development* Open Access option.

© 2021 Kumar et al. This article, published in *Genes & Development*, is available under a Creative Commons License (Attribution 4.0 International), as described at <http://creativecommons.org/licenses/by/4.0/>.

Clerici et al. 2017; Sun et al. 2018). The structures also provided a rationale for how WDR33 and CPSF30 (Yth1 in yeast) bind specific sequences in RNA (Clerici et al. 2018; Sun et al. 2018).

Fip1 and Pap1 interact directly, and a crystal structure of yeast Pap1 bound to residues 80–105 of Fip1 provided the molecular details of their interaction (Meinke et al. 2008). Fip1 has also been reported to interact with other CPF and CF IA components such as Pta1, Yth1, and Rna14 (Preker et al. 1995; Barabino et al. 2000; Ohnacker et al. 2000; Tachashi et al. 2003; Ghazy et al. 2009; Casañal et al. 2017) but neither Fip1 nor Pap1 was visible in cryoEM studies. Fip1 has an N-terminal acidic stretch and a C-terminal Pro-rich region (Preker et al. 1995; Kaufmann et al. 2004). These overall properties of Fip1 are conserved, but human FIP1 (hFIP1) is longer and additionally contains C-terminal Arg-rich and Arg/Asp-rich domains compared with the yeast ortholog (Kaufmann et al. 2004). Biochemical and genetic experiments led to the hypothesis that Fip1 is an unstructured protein that acts as a flexible linker between Pap1 and CPF (Meinke et al. 2008; Ezeokonkwo et al. 2011). Very recently, a crystal structure of human CPSF30 bound to hFIP1 was reported (Hamilton and Tong 2020). This showed that CPSF30 binds two copies of hFIP1 with its zinc fingers 4 and 5. However, Fip1 structure has only been studied in isolation or in complex with Pap1 or Yth1; whether Fip1 remains dynamic in the context of the entire 14-subunit CPF remains unclear.

The nuclease module subunits are flexibly positioned with respect to the polymerase module (Hill et al. 2019; Zhang et al. 2020), but they are hypothesized to become fixed upon CPF activation (Sun et al. 2020). It is likely that the enzymes of CPF are regulated at several levels: First the nuclease must be activated. Second, the nuclease must be inactivated after cleavage has occurred. Finally, the RNA must be transferred to Pap1's active site to allow the poly(A) tail to be synthesized to the correct length. Conformational changes associated with regulation and function of multiprotein complexes frequently involve dynamic IDRs (Fuxreiter et al. 2014; van der Lee et al. 2014); however, it remains unknown whether CPF has different conformational states and whether flexible IDRs contribute to CPF function.

Here, we aimed to understand the function and dynamics of Fip1 using biochemical reconstitution, biophysical experiments, and NMR spectroscopy. We found that isolated Fip1 is an intrinsically disordered protein in solution, with defined binding sites for Yth1 and Pap1 that are connected by a low-complexity sequence. To fully characterize Fip1 as an essential component of the CPF, we reconstituted a recombinant 850-kDa CPF. This allowed us to incorporate an isotopically labeled Fip1 into CPF for NMR studies, in which we show that, with the exception of the Yth1- and Pap1-binding sites, Fip1 remains dynamic and largely disordered within CPF. Moreover, deletion of a highly flexible region in Fip1 impairs CPF nuclease activity. Together, our data reveal that Fip1 dynamics are important in regulating eukaryotic mRNA 3' end processing.

## Results

### *Yth1 binds Fip1, which in turn tethers Pap1 to the polymerase module*

To investigate how Fip1 and Pap1 interact with other CPF subunits, we first studied the five-subunit polymerase module purified from a baculovirus-mediated insect cell overexpression system as previously described (Casañal et al. 2017). We used cryoEM to image this five-subunit complex (Supplemental Fig. S1). Selected 2D class averages show a central structure that resembles the Cft1-Pfs2-Yth1 scaffold identified previously in the four-subunit complex lacking Pap1 (Fig. 1A; Casañal et al. 2017). In addition, a horseshoe-shaped structure was present in the 2D class averages at several different positions relative to Cft1-Pfs2-Yth1. This extra density resembles a 2D projection of the crystal structure of Pap1 (Bard et al. 2000), suggesting that Pap1 is positioned flexibly with respect to the Cft1-Pfs2-Yth1 scaffold. The lack of a defined position for Pap1 precluded high-resolution structure determination.

Next, to gain further insight into the architecture of the polymerase module, we investigated subunit interactions using pull-down assays. Using a StrepII tag on Pfs2, all five subunits were copurified (Fig. 1B). When we removed Pap1 from the complex, the four remaining subunits were still associated. However, removal of Fip1 resulted in concomitant loss of Pap1 from the complex (Fig. 1B). Thus, Fip1 is essential for Pap1 association with the polymerase module and, if it is flexible, it may contribute to the variable positioning of Pap1 in EM images (Fig. 1A).

Fip1 is hypothesized to bind Yth1, which contains five zinc fingers. The N-terminal half of Yth1, including zinc fingers 1 and 2, interacts with Cft1 and Pfs2 (Casañal et al. 2017), zinc fingers 2 and 3 interact with RNA (Clerici et al. 2018; Sun et al. 2018), and, in humans, zinc fingers 4 and 5 interact with hFIP1 (Hamilton and Tong 2020). The C-terminal half of Yth1 is not visible in cryoEM maps, suggesting that it may be flexible. To test whether the C-terminal region is required for interaction with other polymerase module subunits, we carried out pull-down assays with versions of Yth1 containing C-terminal deletions. Deletion of the C-terminal half of Yth1, spanning zinc finger 4, zinc finger 5, and a C-terminal helical region, resulted in a complete loss of Fip1 and Pap1 association with the complex. Deletion of zinc finger 5 and the C-terminal helical region reduced, but did not abolish, the association of Fip1 and Pap1 from the Pfs2 pull-downs. Deletion of zinc finger 4 resulted in loss of Pap1, but a weak band corresponding to a protein the size of Fip1 was still present (Fig. 1B). There are a number of additional bands present in this pull-down that may represent Pfs2 degradation products. This suggests that deletion of Yth1 zinc finger 4 compromises the stability of the complex. Given that Pap1 is absent when zinc finger 4 is deleted, the 50-kDa band may be a degradation product of Pfs2. Based on these data, we hypothesize that Yth1 zinc finger 4 is the major binding site for Fip1 and is required for Fip1 (and Pap1) incorporation into the fully recombinant polymerase module, in agreement with a previously proposed

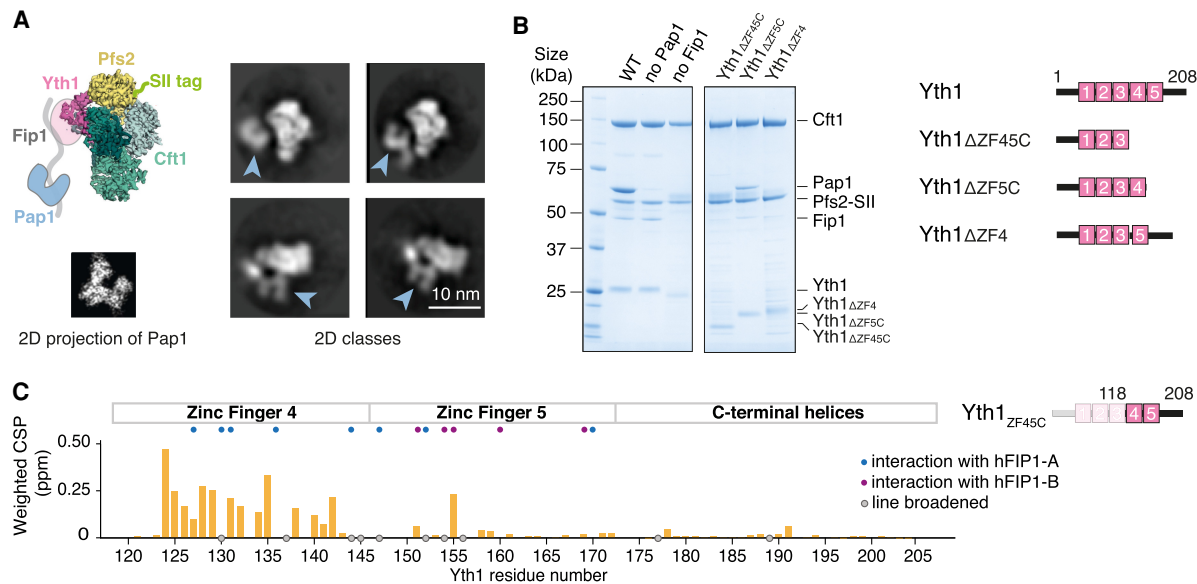


**Figure 1.** Fip1 binds Yth1 and tethers Pap1 to the polymerase module. (A) Cartoon representation (top left) and selected 2D class averages from cryoEM (right) of the polymerase module. The 2D averages show a central structure corresponding to the Cft1-Pfs2-Yth1 subunits, and an additional horseshoe-shaped density (blue arrowheads). (Bottom left) Similarity to a 2D projection of the crystal structure of Pap1 (PDB 3C66) suggests that the horseshoe-shaped density is Pap1. (SII) StrepII. (B) SDS-PAGE of pull-down assays using StrepII-tagged (SII) Pfs2 reveals interactions within the polymerase module. (Right) Domain diagrams of Yth1 indicate the constructs used. Fip1 is required for Pap1 interaction. When the interaction between Yth1 and Fip1 is compromised, Fip1 is not pulled down and therefore Pap1 is also absent. Yth1 subunits in the WT and "no Pap1" complexes contain a His tag, whereas Yth1 in the "no Fip1" and Yth1 truncation complexes do not contain a His tag. With Yth1 $\Delta$ ZF4, protein degradation (potentially from Pfs2) is evident. (C) Histogram showing chemical shift perturbations (CSPs) in Yth1 $\Delta$ ZF45C (residues 118–208) spectra upon Fip1 $\Delta$ 226 binding. Yth1 $\Delta$ ZF45C and Fip1 $\Delta$ 226 were mixed in an equimolar ratio to a final concentration of 75  $\mu$ M. Gray circles indicate peaks that showed exchange broadening upon Fip1 binding. Most of the peaks that are perturbed are in zinc finger 4. Homologous residues contributing  $>50 \text{ \AA}^2$  buried surface area in the human FIP1-CPSF30 structure (Hamilton and Tong 2020) are highlighted with blue or purple circles. In that structure, two hFIP1 molecules (hFIP1-A and hFIP1-B) are bound to one CPSF30.

role for this zinc finger in Fip1 binding (Takahashi et al. 2003; Hamilton and Tong 2020). Zinc finger 5 may contain a low-affinity binding site for Fip1.

To characterize the Yth1-Fip1 interaction, we performed NMR analysis of two Yth1 constructs: the entire C-terminal half (Yth1 $\Delta$ ZF45C; residues 118–208) or zinc finger 4 on its own (Yth1 $\Delta$ ZF4; residues 118–161) (Supplemental Fig. S2A–C). We assigned backbone resonances of Yth1 $\Delta$ ZF45C and mapped chemical shift perturbations upon addition of a Fip1 construct containing residues 1–226 (Fip1 $\Delta$ 226) (Fig. 1C; Supplemental Fig. S2D). (Details on the choice of Fip1 $\Delta$ 226 construct are described in the next section.) Addition of Fip1 $\Delta$ 226 resulted in substantial chemical shift perturbations and line broadening. The majority of changes (19 out of 25 residues experiencing chemical shift perturbation or line broadening) are located within residues in zinc finger 4, with a similar pattern in both Yth1 $\Delta$ ZF45C and Yth1 $\Delta$ ZF4 spectra. The remaining changes are located in zinc finger 5. Thus, Yth1 zinc finger 4 is the primary interaction site for Fip1.

There are apparent domain boundaries on either side of Yth1 zinc finger 4, but this region contains very little secondary structure (Supplemental Fig. S2E,F). We confirmed a direct interaction of Yth1 $\Delta$ ZF4 and Fip1 $\Delta$ 226 using isothermal calorimetry, with a measured binding affinity of 240

nM  $\pm$  40 nM (Supplemental Fig. S2G). Fip1 $\Delta$ 226 binds more tightly to the Yth1 $\Delta$ ZF45C construct, in agreement with zinc finger 5 also making contributions to the binding site (Supplemental Fig. S2H,I). We found that zinc finger 4 in Yth1 $\Delta$ ZF45C loses its structure upon incubation with EDTA, suggesting that the zinc ions are exposed and susceptible to metal chelation in the free protein (Supplemental Fig. S2J). Interestingly, addition of EDTA results in minimal changes in the Yth1 $\Delta$ ZF45C spectra in the presence Fip1 $\Delta$ 226 (Supplemental Fig. S2K). Therefore, Fip1 renders the Yth1 $\Delta$ ZF45C zinc fingers resistant to loss of metal coordination. Taken together, Fip1 directly interacts with and stabilizes Yth1.

#### Fip1 is largely disordered in solution

Next, we examined the structure of Fip1. We first performed bioinformatics analyses on the sequence features of the full-length, 327-amino-acid protein (Fig. 2A). Overall,  $>75\%$  of Fip1 ( $\sim 250$  residues) is predicted to be highly disordered, including an N-terminal serine-rich acidic region (residues 1–60), a central low-complexity region (LCR) rich in serine and threonine (residues 110–180), and a C-terminal region with no net charge that is enriched in asparagine, proline, and phenylalanine (residues

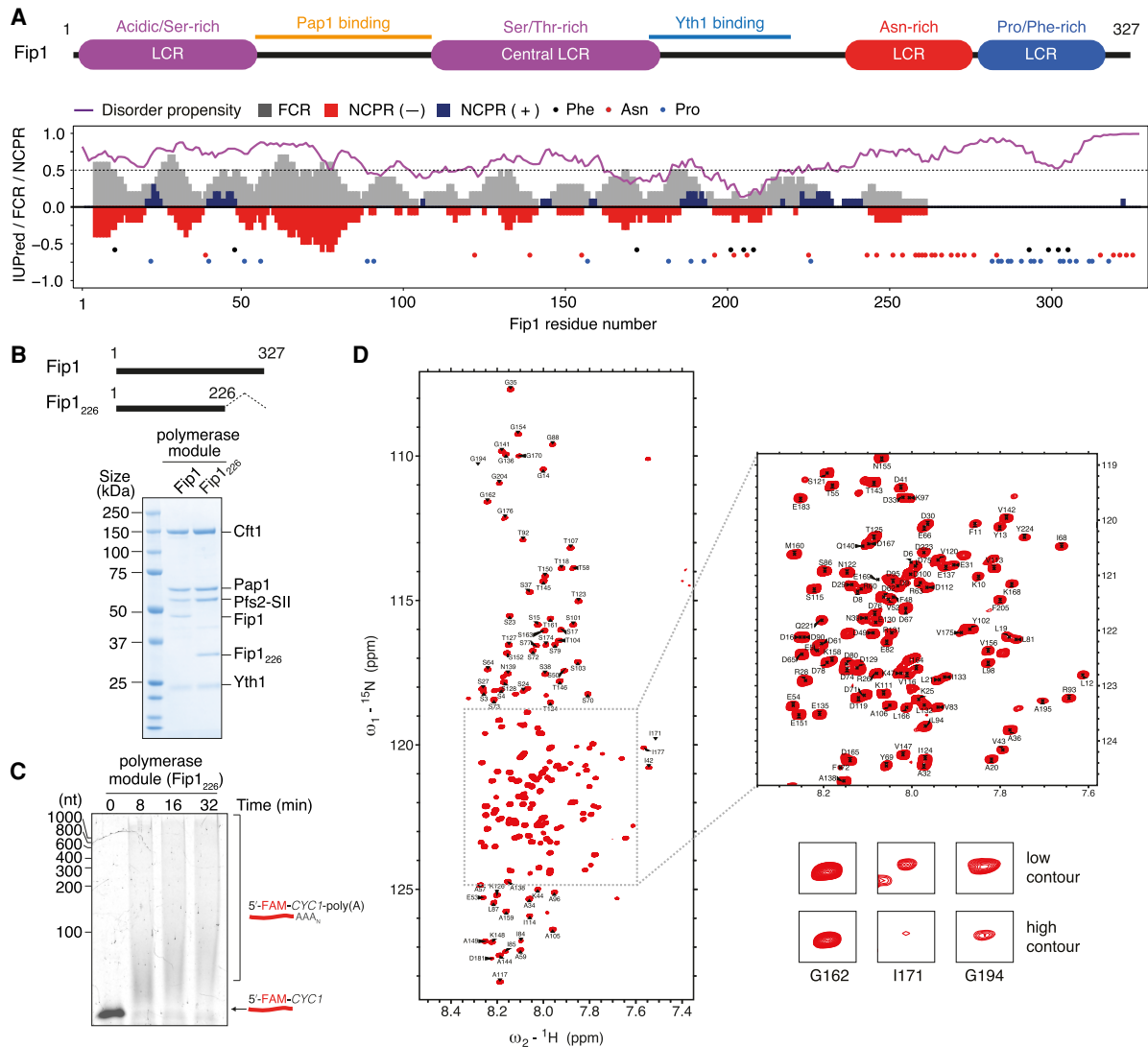


**Figure 2.** Fip1 residues 1–226 are sufficient for reconstitution of the polymerase module. (A) Domain diagram of Fip1 showing low-complexity regions (LCRs), Pap1-binding site, and Yth1-binding site (top), and bioinformatic analysis of the Fip1 sequence (bottom). In the plot, the purple line indicates IUPRED disorder prediction score. Residues with an IUPRED value >0.5 (gray dotted line) are classified as having high propensity for being intrinsically disordered. Gray bars correspond to fraction of charged residues (FCR) over a sliding window of 10 residues. Red and blue bars represent net negative and positive charge per residue (NCPR), respectively, over the same window size. The colored circles highlight the distribution of phenylalanine (black), asparagine (red), and proline (blue) residues. (B) Schematic showing construct design of Fip1<sub>226</sub> (residues 1–226; top) and SDS-PAGE of pull-down assays of a polymerase module using StrepII-tagged (SII) Pfs2 3' (bottom). (C) In vitro polyadenylation assay with a recombinant polymerase module containing Fip1<sub>226</sub>. A 42-nucleotide *CYC1* 3' UTR with a 5'-FAM label was used as a substrate in the polyadenylation assay, and the reaction products were visualized on a denaturing urea polyacrylamide gel. This gel is representative of experiments performed twice. (D) <sup>1</sup>H, <sup>15</sup>N 2D HSQC of 75 μM Fip1<sub>226</sub> shown with the assignment of backbone resonances. The inset highlights a crowded region of the spectra. The bottom panels show examples of peaks. I171 and G194 show line broadening. BEST <sup>1</sup>H, <sup>15</sup>N-TROSY spectra were acquired with four scans and a recycle delay of 400 msec, giving a final spectral resolution of 0.9 Hz per points in the indirect dimension and an experimental time of 20 min.

243–327). This is consistent with previous evidence that isolated Fip1 is largely unfolded (Meinke et al. 2008; Ezeokonkwo et al. 2011). Interestingly, the only region that is predicted to have low disorder propensity (residues 193–215) overlaps with sequences previously identified as important for Yth1 binding (residues 206–220) (Helmeling et al. 2001) and is highly conserved across eukaryotes (Supplemental Fig. S3A). The N-terminal region contain-

ing the previously described Pap1-binding site (residues 80–105) is not highly conserved (Supplemental Fig. S3A). This is consistent with previous reports that the molecular details of the interaction between Pap1 and Fip1 are not important for Pap1's activity, but physical tethering is important (Ezeokonkwo et al. 2011).

The C-terminal region of Fip1 is poorly conserved compared with the N-terminal region, both in length and in

amino acid composition (Supplemental Fig. S3B), suggesting that the C-terminal region may not be crucial to the function of Fip1. A previous study showed that deletion of residues 220–327 had negligible effect on the viability of yeast cells and no substantial effect on mRNA polyadenylation *in vitro* (Helmling et al. 2001). Since overexpression of isolated full-length Fip1 resulted in insoluble protein aggregates, we removed residues 227–327, which contain the aggregation-prone Asn-rich region, to create a Fip1<sub>226</sub> construct that is stable for *in vitro* characterization. As a helical stretch is predicted close to the truncation point, we chose proline 226 as a natural helix breaker for the new C terminus.

We coexpressed Fip1<sub>226</sub> with the other polymerase module subunits in *Sf9* insect cells and performed pull-down assays using the StrepII tag on Pfs2 (Fig. 2B). This showed that Fip1<sub>226</sub> is incorporated into the recombinant polymerase module. This complex was active in *in vitro* polyadenylation assays (Fig. 2C). Together, this shows that residues 1–226 are sufficient for Fip1 incorporation into the polymerase module and for polyadenylation activity, confirming our prediction that residues beyond 226 on Fip1 are not essential for cleavage and polyadenylation.

Next, we analyzed Fip1<sub>226</sub> using NMR. Several regions contain substantial signal attenuation due to line broadening, including residues between 170 and 220 (Materials and Methods; Supplemental Fig. S3C,D). We assigned 187 out of 226 (83%) backbone resonances (Fig. 2D). Although several regions have some propensity to form secondary structure (Supplemental Fig. S3E), Fip1<sub>226</sub> generally has a narrow <sup>1</sup>H dispersion in a <sup>1</sup>H, <sup>15</sup>N 2D HSQC spectrum (Fig. 2D), consistent with Fip1 being a largely disordered protein in solution.

#### *Fip1 contains independent binding sites for Yth1 and Pap1*

IDRs can either become ordered or remain dynamic upon binding to other subunits in a multiprotein complex (Fuxreiter et al. 2014; van der Lee et al. 2014). To understand the conformational state of Fip1 and its contribution to CPF function, we investigated the dynamics of Fip1 when bound to other subunits. We first sought to identify the interaction sites for polymerase module subunits within Fip1 by making deletions in Fip1 and performing pull-down assays using the StrepII tag on Pfs2 (Fig. 3A). Residues 80–105 had previously been shown to mediate Fip1 interaction with Pap1 (Meinke et al. 2008) and therefore we did not assess that region in pull-down assays. We found that Fip1 residues 190–220 are required for Fip1 (and Pap1) interaction with the polymerase module. In contrast, deletion of the N-terminal acidic region (residues 1–60) or the central LCR (residues 110–180) had minimal effect on Fip1 interactions. These experiments therefore suggest that Fip1 residues 190–220 interact with Yth1 to promote association with the polymerase module.

Next, we used NMR to gain residue-level insight into the molecular interactions of both Yth1 and Pap1 with Fip1. We incubated Fip1<sub>226</sub> with Yth1<sub>ZF4</sub>, Pap1, or Yth1<sub>ZF4</sub> and Pap1 together, and mapped the changes in the spectra

(Fig. 3B; Supplemental Fig. S4A). First, upon incubation with Yth1<sub>ZF4</sub>, major chemical shift perturbations and substantial line broadening were observed for resonances corresponding to Fip1 residues 170–220, indicating a potential interaction between this region and Yth1<sub>ZF4</sub> (Fig. 3B, top). This region had also exhibited intrinsic line broadening in the absence of Yth1<sub>ZF4</sub> (Supplemental Fig. S3D,E). Therefore, we used <sup>13</sup>C-detect CON studies using deuterated Fip1<sub>226</sub>. Although the signal intensities were reduced in the <sup>13</sup>C-detect experiments due to the lower gyromagnetic ratio of <sup>13</sup>C, line broadening was reduced by avoiding proton detection. These experiments provide an additional advantage of improved chemical shift dispersion for intrinsically disordered proteins. We could then unambiguously define additional signals for C-terminal residues, providing an independent confirmation that residues 180–220 are involved in Yth1 binding (Supplemental Fig. S4B,C). Together, these data revealed that the major Yth1-binding site on Fip1 is within residues 180–220.

Next, upon incubation with unlabeled 66-kDa Pap1, chemical shift perturbations were observed for signals within Fip1<sub>226</sub> residues 58–80, and signal attenuation as a result of line broadening was observed for resonances within residues 66–110 (Fig. 3B, middle). In addition, some resonances from the N-terminal acidic region were slightly perturbed upon Pap1 binding, which may be the result of charge–charge interactions. Together, our observations are in agreement with binding of Fip1 residues 80–105 to Pap1, as observed in the crystal structure (Meinke et al. 2008), but also suggest that additional Fip1 residues (58–110) participate in the interaction. Interestingly, previous studies had shown that Pap1 has higher affinity for full-length Fip1 than for residues 80–105 (Meinke et al. 2008), consistent with involvement of additional residues in this interaction.

Finally, when both Yth1<sub>ZF4</sub> and Pap1 were added to labeled Fip1<sub>226</sub>, the binding patterns of each individual protein were retained (Fig. 3B, bottom). This suggests that Fip1 contains two independent binding sites: one for Yth1 and one for Pap1. Interestingly, the central LCR was not involved in either of these interactions. Most of the central LCR remains unperturbed, suggesting that this region is still largely disordered and highly dynamic, even when Fip1 is bound to Pap1 and Yth1.

#### *Reconstitution of a fully recombinant CPF*

Residues 110–170 within the central LCR of Fip1 remain dynamic in the presence of Yth1<sub>ZF4</sub> and Pap1, raising the possibility that they could also be dynamic in the context of the full CPF complex. To investigate this and dissect the structural nature of Fip1 in CPF, we established a strategy to purify a fully recombinant CPF complex containing all 14 subunits with selectively labeled Fip1<sub>226</sub> that could be used for NMR analysis. Previous biochemical studies used native CPF purified from yeast (Casañal et al. 2017). The recombinant system greatly simplifies genetic manipulation of CPF.

We used a modified version of the biGbac system (Weissmann et al. 2016; Hill et al. 2019) to produce two

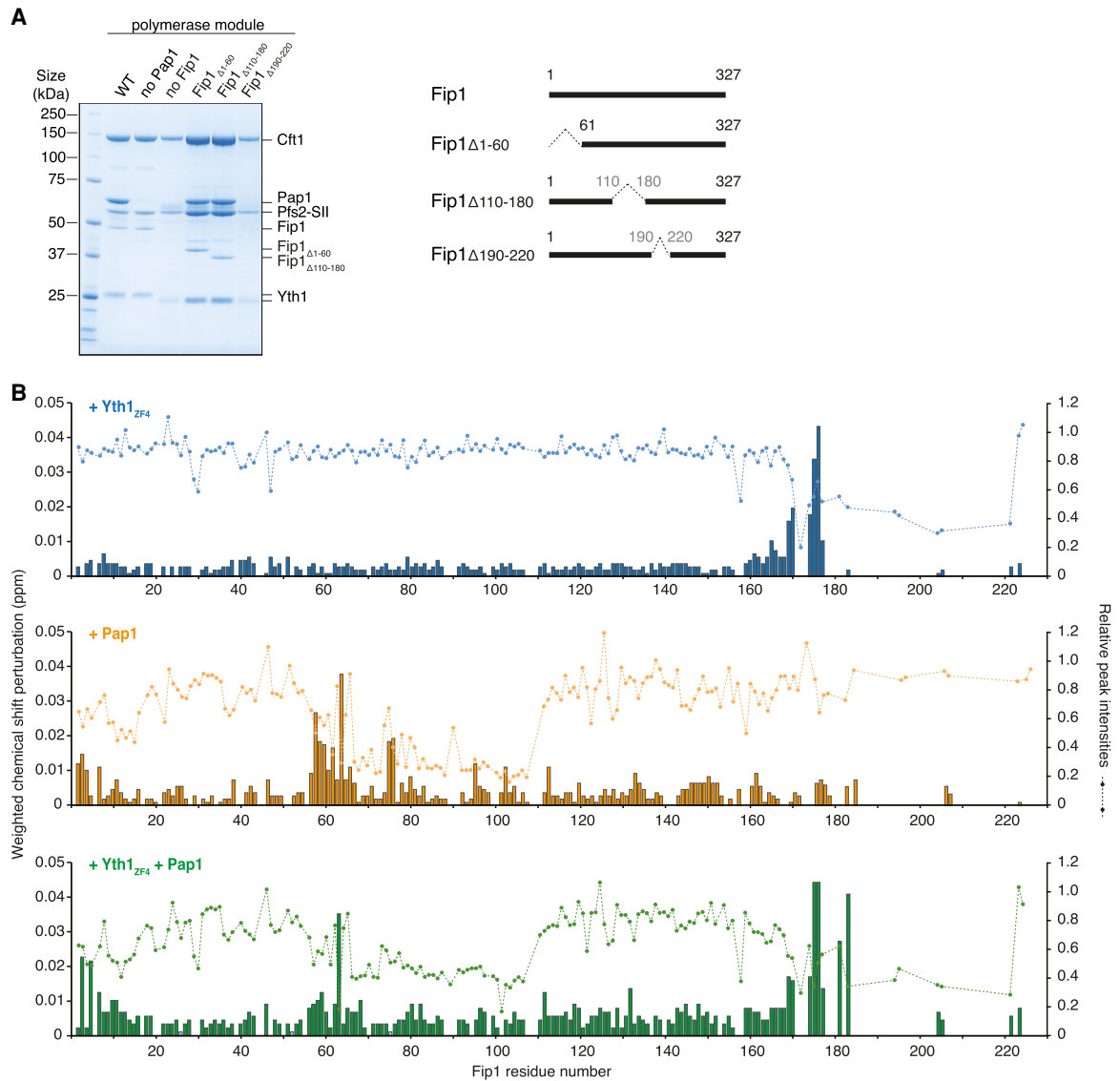


**Figure 3.** Fip1<sub>226</sub> contains bipartite binding sites for Yth1 and Pap1. (A) SDS-PAGE of pull-down assays using StrepII-tagged (SII) Pfs2. Residues 190–220 on Fip1 are essential for reconstitution of the polymerase module. Yth1 is 6His-tagged for wild-type (WT) and “no Pap1” samples, but untagged in all other samples. Diagrams of full-length and truncated Fip1 are shown at the right. The first three lanes (WT, no Pap1 and no Fip1) are reproduced from Figure 1B. (B) Chemical shift perturbations of Fip1<sub>226</sub> upon binding of Yth1<sub>ZF4</sub> (blue, top), Pap1 (orange, middle), and Yth1<sub>ZF4</sub> and Pap1 together (green, bottom). Chemical shift perturbations are shown as histograms. The dotted line indicates the relative peak intensities compared with free Fip1<sub>226</sub> in the <sup>1</sup>H, <sup>15</sup>N 2D HSQC spectra. Experiments were performed at 150 mM NaCl to minimize potential nonspecific binding.

bacmids: One bacmid contained genes encoding the eight subunits of the nuclease and polymerase modules, and a second bacmid contained the six genes encoding the phosphatase module (Supplemental Fig. S5A). These two bacmids were used for coinfection of *Sf9* cells and the complex was purified using a StrepII tag on the Ref2 subunit. The isolated complex was then subjected to anion exchange chromatography followed by size exclusion chromatography (Supplemental Fig. S5B). SDS-PAGE analysis of the purified CPF showed the presence of all 14 subunits (Fig. 4A; Supplemental Fig. S5C). Size exclusion chromatography coupled with multiangle light scat-

tering (SEC-MALS) revealed a molecular weight of 879 kDa  $\pm$  28 kDa, which is in agreement with the theoretical molecular weight of CPF (860 kDa) with all subunits in uniform stoichiometry (Supplemental Fig. S5D). We also tested *in vitro* cleavage and polyadenylation activities to determine whether the complex is functionally active. Recombinant CPF specifically cleaves the 3' UTR of a model pre-mRNA and polyadenylates the cleaved RNA product (Fig. 4B). Thus, we were able to purify a fully recombinant, active CPF.

Next, we produced a variant of CPF lacking Fip1 (referred to as CPF $\Delta$ Fip1) using the same method

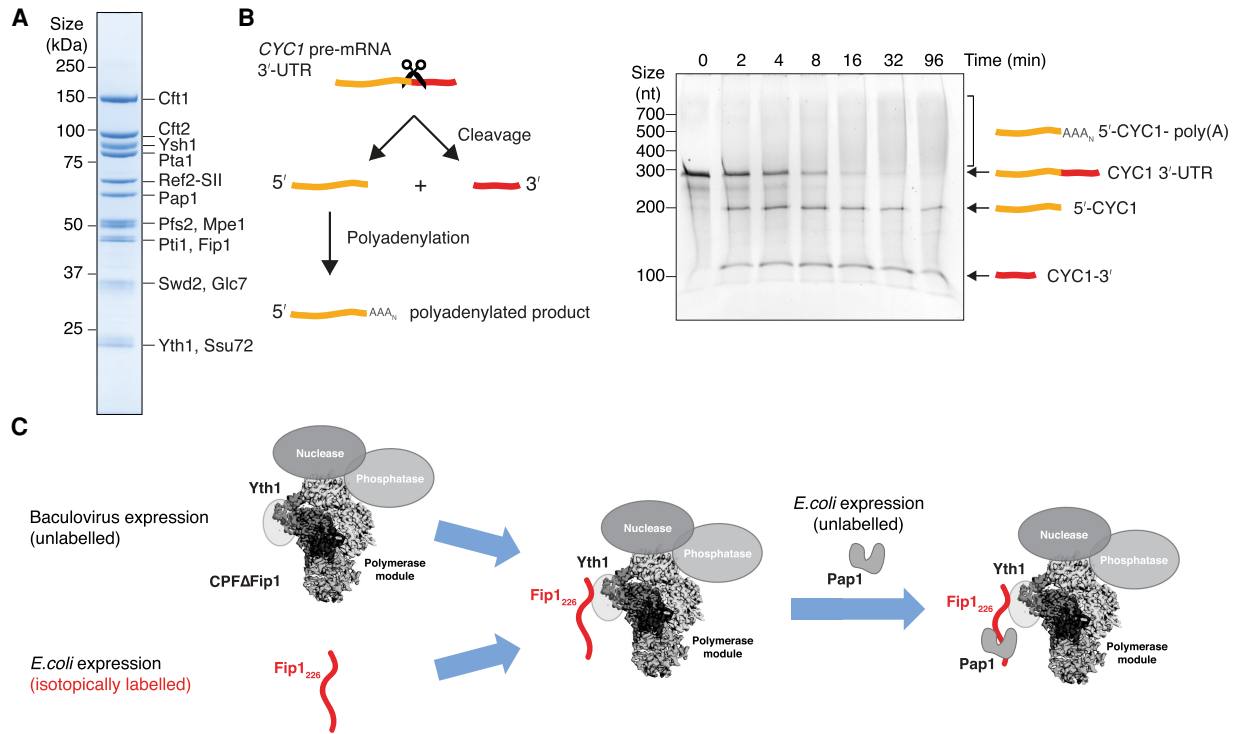


**Figure 4.** Purification of a recombinant, active CPF. (A) SDS-PAGE showing all 14 subunits present in purified recombinant CPF. (SII) StrepII affinity tag. (B) Schematic diagram (left) and denaturing urea polyacrylamide gel (right) of cleavage and polyadenylation assay of recombinant CPF. A 259-nt *CYC1* 3' UTR was used as a model pre-mRNA substrate. This gel is representative of experiments performed twice. (C) Workflow for preparing CPF with selectively labeled Fip1<sub>226</sub>. Recombinant CPFΔFip1 was purified from baculovirus expression, while isotopically labeled Fip1<sub>226</sub> was purified after overexpression in *E. coli*. Purified Fip1<sub>226</sub> was combined with excess CPFΔFip1 (1:1.1) and the resulting complex was used for NMR analysis. Free CPFΔFip1 is silent in NMR experiments, as it is unlabeled. Excess Pap1 was added to study its interaction with Fip1 on CPF.

(Supplemental Fig. S5E). Notably, Pap1 was also absent, showing that, like in the polymerase module, Fip1 is essential for Pap1 incorporation into intact CPF. We separately expressed and purified isotopically labeled Fip1<sub>226</sub> from *E. coli*. To make a selectively labeled CPF-Fip1<sub>226</sub> chimeric complex for NMR analysis, we mixed unlabeled CPFΔFip1 in 1.1-fold excess with isotopically labeled Fip1<sub>226</sub> (Fig. 4C). The small excess of CPFΔFip1 is not visible by NMR and therefore does not contribute to signals observed in the NMR experiments. Finally, we also added excess Pap1 to study the interaction between Pap1 and CPF-Fip1<sub>226</sub>.

To monitor the integrity and stoichiometry of these complexes, we used mass photometry. By measuring the light scattered by single molecules, mass photometry can be used to determine molecular mass with minimal amounts of protein (10  $\mu$ L of 100 nM samples) (Young et al. 2018). Mass photometry reported a molecular mass in the range of  $\sim$ 850 kDa for recombinant CPF (Supplemental Fig. S5F), which is in agreement with the expected mass and the SEC-MALS measurement (Supplemental Fig. S5D). Additionally, the reported molecular masses for CPFΔFip1, CPF-Fip1<sub>226</sub>, and CPF-Fip1<sub>226</sub>-Pap1 are all in good agreement with their expected molecular masses (Supplemental Fig. S5F), confirming stable reconstitution of these complexes. These data show that we were able to

generate NMR samples of  $\sim$ 10  $\mu$ M selectively labeled Fip1<sub>226</sub>-CPF.

#### *Fip1 is largely dynamic in the intact CPF complex*

To investigate the dynamics of Fip1 when it is incorporated into CPF, we used NMR to study the recombinant complex. As this complex is  $\sim$ 1 MDa in size, we used a combination of  $^2\text{H}$ ,  $^{13}\text{C}$ ,  $^{15}\text{N}$  selectively labeled samples and BEST  $^1\text{H}$ ,  $^{15}\text{N}$ -TROSY experiments to enhance sensitivity. Spectra of CPF-Fip1<sub>226</sub> were compared with spectra of free Fip1<sub>226</sub> at the same concentration of 11  $\mu$ M (Fig. 5A). Strikingly, even in the spectra of the 850-kDa complex, Fip1<sub>226</sub> signals can be clearly observed, indicating that a large proportion of Fip1 remains highly dynamic when bound to CPF. To ensure the signals in the CPF-Fip1<sub>226</sub> spectra corresponded to CPF-bound Fip1<sub>226</sub> and not to free Fip1<sub>226</sub>,  $^{15}\text{N}$ -edited  $^1\text{H}$  diffusion experiments were used to determine the diffusion coefficients of the  $^{15}\text{N}$ -labeled species in the samples (Supplemental Fig. S6). The measured diffusion coefficient of Fip1<sub>226</sub> alone ( $4.6 \times 10^{-11} \text{ m}^2\text{sec}^{-1}$ ) is consistent with a highly mobile, free protein, whereas the diffusion coefficient of CPF-Fip1<sub>226</sub> ( $2.8 \times 10^{-11} \text{ m}^2\text{sec}^{-1}$ ) is consistent with a larger, more slowly diffusing CPF-bound species. Along with the pull-down and mass photometry data (Supplemental

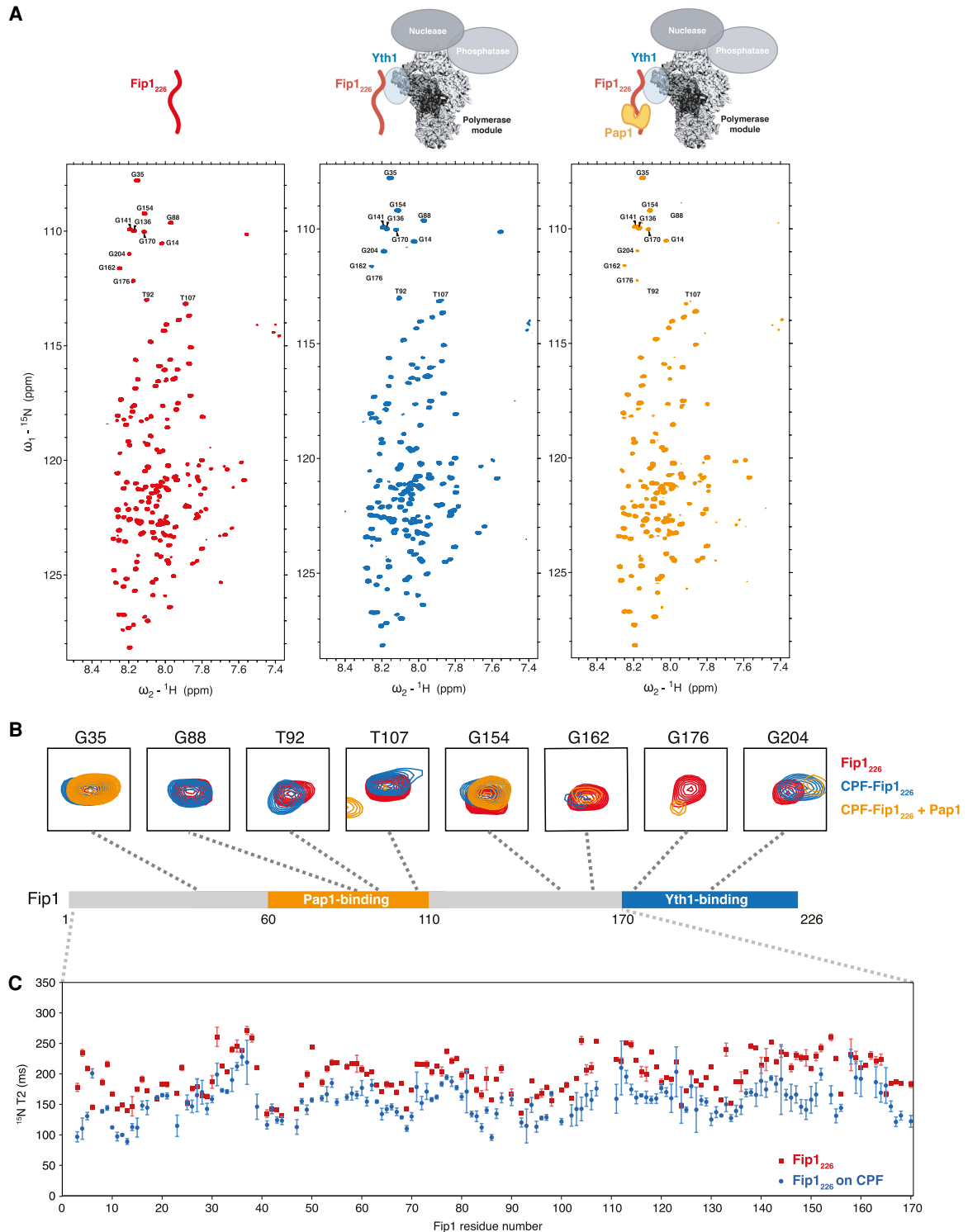


**Figure 5.** The LCRs of Fip1<sub>226</sub> are highly dynamic within the CPF complex. (A) <sup>1</sup>H, <sup>15</sup>N 2D HSQC of Fip1<sub>226</sub>, alone (red, *left*) and bound to CPFΔFip1 (blue, *middle*) or CPFΔFip1 and Pap1 (orange, *right*). Schematic diagrams show the proteins included in each experiment. All spectra were collected at 950 MHz with 11 μM <sup>13</sup>C, <sup>15</sup>N, <sup>2</sup>H Fip1<sub>226</sub> in 150 mM NaCl buffer. Peaks analyzed in B are indicated in the spectra. BEST <sup>1</sup>H, <sup>15</sup>N-TROSY spectra were acquired with 64 scans and a recycle delay of 400 msec, giving a final spectral resolution of 2.2 Hz per point in the indirect dimension and an experimental time of 142 min. (B) Selected Fip1<sub>226</sub> peaks for all three samples. Perturbation or line broadening of peaks specific to the defined regions for Yth1 and Pap1 binding was observed upon interaction with CPFΔFip1 and Pap1. Peaks are mapped onto a diagram of the Fip1<sub>226</sub> protein. Colors as in A. (C) T<sub>2</sub> relaxation data for the first 170 residues of Fip1<sub>226</sub> alone (red) and incorporated into CPFΔFip1 (blue).



Fig. S5D–F), this shows that the CPF-Fip1<sub>226</sub> complex is stable and intact during NMR data acquisition.

In general, the narrow dispersion of proton chemical shifts in spectra of CPF-Fip1<sub>226</sub> and free Fip1<sub>226</sub>, and the relatively narrow line widths suggest regions of high local flexibility. This is consistent with Fip1<sub>226</sub> being largely disordered, both when it is free in solution and when it is incorporated into CPF without Pap1. The exception to this is resonances from residues 170–226, which include the Yth1-binding region of Fip1: These residues show selective line broadening in CPF-Fip1<sub>226</sub> and therefore likely become ordered in the complex (Supplemental Fig. S7A). For example, within this region, the peaks for G176 become much weaker and G204 undergoes chemical shift perturbation when Fip1<sub>226</sub> is incorporated into CPF (Fig. 5B). These data indicate that Fip1<sub>226</sub> interacts with Yth1 via residues 170–226 to form a stable complex with CPFΔFip1. In agreement with this, Fip1 residues S198, D199, Y200, N202, Y203, and W210 are implicated in Yth1 binding based on the recently published crystal structure of hFIP1 bound to CPSF30 (Hamilton and Tong 2020). Other regions of Fip1 are relatively unaffected by incorporation into CPF and remain flexible.

When excess Pap1 was added to CPF-Fip1<sub>226</sub>, selective line broadening and chemical shift perturbations were also observed for resonances in the Pap1-binding region (residues 60–110) (Supplemental Fig. S7A). For example, resonances for G88, T92, and T107 disappear or undergo chemical shift perturbation upon addition of Pap1 (Fig. 5B). This confirms that, similar to the isolated proteins (Fig. 3B), interaction between Pap1 and Fip1 within CPF likely extends beyond the region observed in the previously reported crystal structure (Meinke et al. 2008).

Outside the Yth1- and Pap1-binding sites, sharp resonances are present in the CPF-Fip1<sub>226</sub>-Pap1 spectra. These likely represent highly flexible residues in Fip1 and suggest that Fip1<sub>226</sub> does not have any additional major interactions with CPF. To investigate its dynamics, we determined the <sup>15</sup>N transverse relaxation times (*T*<sub>2</sub>) for free Fip1<sub>226</sub>, Fip1<sub>226</sub>-Yth1<sub>ZF4</sub> and CPF-Fip1<sub>226</sub> (Fig. 5C). Resonances from the residues in the Yth1-binding region show substantial line broadening consistent with being ordered, and were therefore not included in this analysis. We found that the interaction of Fip1 with CPF or free Yth1<sub>ZF4</sub> does not substantially alter the flexibility of the first 170 residues of Fip1<sub>226</sub> (Fig. 5C; Supplemental Fig. S7B). We also analyzed the flexibility of Fip1<sub>226</sub> in the presence of Pap1 (Supplemental Fig. S7B). This showed that the Pap1-binding site becomes more rigid upon Pap1 binding, but the residues outside the Pap1-binding site remain highly dynamic. In conclusion, outside the Yth1- and Pap1-binding sites, Fip1 is dynamic in the context of CPF.

#### *The central low-complexity region of Fip1 plays a role in cleavage and polyadenylation*

The dynamic central LCR of Fip1 (residues 110–180) between the Pap1- and Yth1-binding sites is of particular interest because it may flexibly tether Pap1 to CPF. This

would be consistent with the flexible position of Pap1 in cryoEM analysis of the polymerase module (Fig. 1A). To identify whether the central LCR is functionally important for the cleavage and polyadenylation activities of CPF, we deleted Fip1 residues 110–180 and purified a CPF(Fip1Δ110–180) complex. SDS-PAGE analysis of purified CPF(Fip1Δ110–180) showed that it contained all 14 subunits in similar stoichiometry to wild-type CPF (Fig. 6A). Thus, the central LCR of Fip1 is not required for assembly of CPF.

Next, we performed in vitro coupled cleavage and polyadenylation assays with both wild-type and mutant complexes. A synthetic 56-nt *CYC1* 3' UTR RNA was used as a model pre-mRNA substrate. 5'-FAM and 3'-Alexa647 fluorescent labels allowed visualization of the two cleavage products and the polyadenylated RNA. Recombinant wild-type CPF cleaves the substrate RNA efficiently and adds a poly(A) tail to the 5' cleavage product (Fig. 6B, left). In contrast, more substrate RNA remains unprocessed at all time points in the assay for CPF(Fip1Δ110–180) compared with wild-type CPF (Fig. 6B, right). These results could be explained by slower endonucleolytic cleavage of the pre-mRNA or slower activation of the nuclease in CPF lacking Fip1 central LCR.

To assess whether the polyadenylation activity is also defective, we performed an uncoupled polyadenylation assay. Using a 42-nt synthetic *CYC1* RNA ending at the cleavage site (pc*CYC1*), we found that CPF(Fip1Δ110–180) has similar polyadenylation activity to wild-type CPF (Fig. 6C). Interestingly, polyadenylation defects were observed in a previous study where residues 106–190 were replaced with another IDR sequence (Ezeokonkwo et al. 2011). However, this replacement removed some of the highly conserved residues within Fip1 (Supplemental Fig. S3A) and therefore may have disrupted Yth1 positioning within the complex. Thus, we replaced residues 110–170 of the Fip1 central LCR with either a scrambled version of the same sequence (Fip1<sub>scramble</sub>) or with an IDR of the same length from another protein, Puf3 (Fip1<sub>Puf3</sub>) (Supplemental Fig. S8). These Fip1 variants were incorporated into CPF and used to assess whether the flexibility, the amino acid composition, or the exact amino acid sequence of the central LCR is important. Interestingly, CPF with either IDR replacement had cleavage and polyadenylation activities that were essentially indistinguishable from wild-type (Supplemental Fig. S8). Together, our in vitro assays show that the Yth1- and Pap1-binding sites on Fip1 must be separated by a flexible linker for efficient pre-mRNA cleavage.

## Discussion

mRNA 3' end processing by CPF is essential for the production of mature mRNA. Here, using in vitro reconstitution and structural studies, we gained new insight into the architecture of CPF. We show that the essential Fip1 subunit contains IDRs that are dynamic, even when Fip1 is incorporated into the full CPF complex. Thus, a large part of Fip1 does not become ordered in apo CPF and

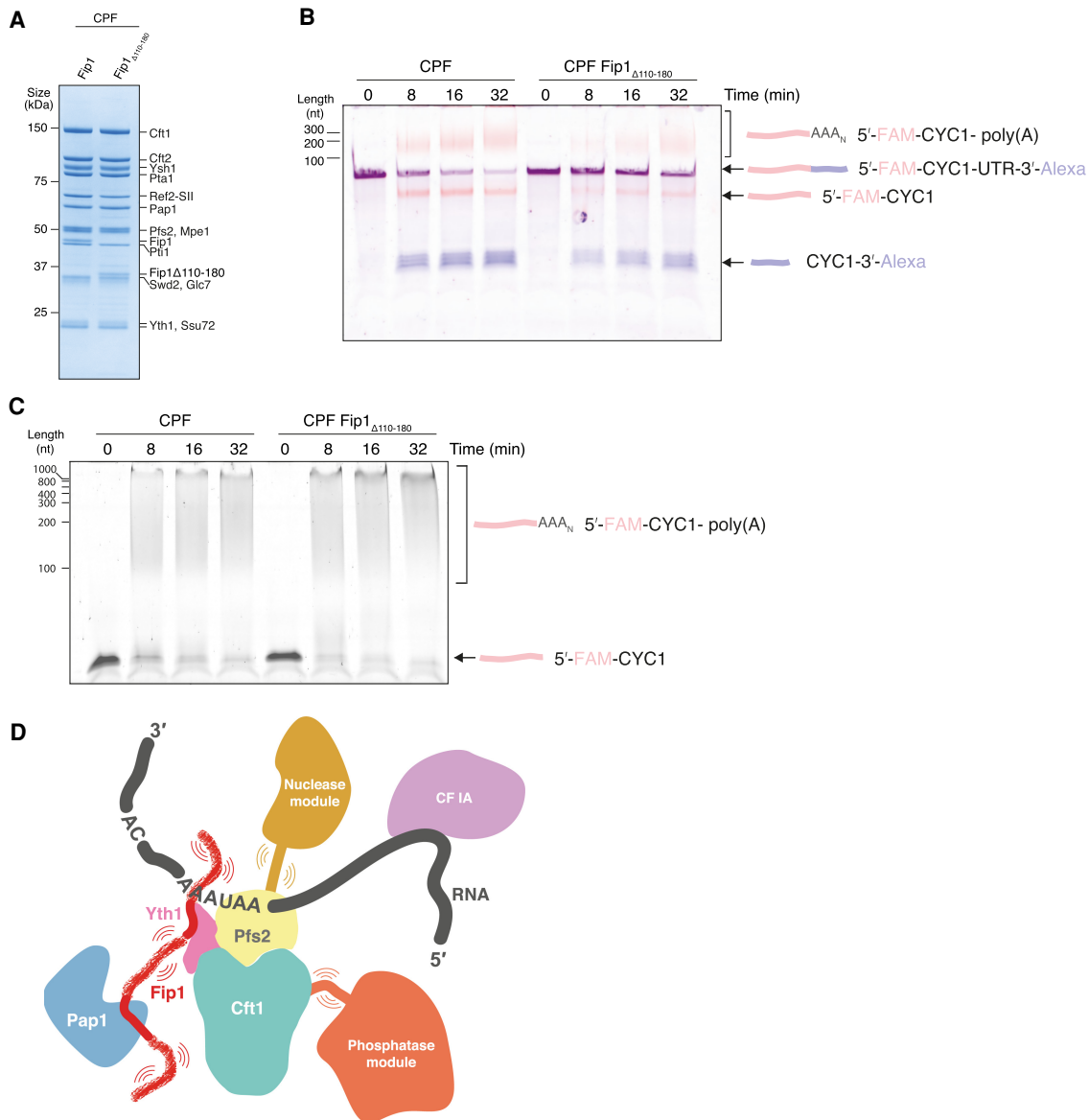


**Figure 6.** The central LCR of Fip1<sub>226</sub> is important for CPF function. (A) SDS-PAGE of purified CPF alongside CPF(Fip1 $\Delta$ 110–180). Deletion of the central LCR in Fip1 does not affect the assembly and purification of CPF. The composition and stoichiometries of CPF subunits are similar in both samples. (B) Denaturing gel electrophoresis of coupled cleavage and polyadenylation assays of a *CYC1* 3' UTR containing a 5'-FAM and a 3'-A647 label. Each reaction contained 50 nM CPF or CPF(Fip1 $\Delta$ 110–180), 100 nM *CYC1* 3'-UTR, and 300 nM CF IA and IB. The cleavage activity of CPF is compromised in the absence of the central LCR in Fip1. This gel is representative of experiments performed twice. (C) Polyadenylation activity of wild-type CPF compared with CPF(Fip1 $\Delta$ 110–180). The RNA contains a 5'-FAM label. This gel is representative of experiments performed twice. (D) Model for CPF. The central IDR of Fip1 flexibly tethers Pap1 to the complex. Additionally, IDRs within other subunits in each of the modules may allow flexibility to permit conformational remodeling.

may be required to impart flexibility between the RNA-binding sites in CPF and the Pap1 enzyme.

#### *Fip1 binds Yth1 zinc finger 4 and Pap1*

Fip1 interacts directly with zinc finger 4 of Yth1 (Fig. 1A, B; Helmling et al. 2001; Tacahashi et al. 2003; Hamilton and Tong 2020) and is proposed to bind additional 3' end processing factors such as Pfs2 and Rna14 (Ohnacker et al. 2000). We identified the Yth1- and Pap1-binding sites

within Fip1 using NMR but there were no major changes in Fip1<sub>226</sub> spectra outside these sequences after Fip1 incorporation into intact CPF. Thus, it appears that Fip1 does not interact with other CPF subunits in this context. Fip1 may acquire new interaction partners (e.g., the Rna14 subunit of CF IA) during CPF activation.

Our previous analysis of native yeast CPF showed that up to two Fip1 and two Pap1 molecules can associate with the complex (Casañal et al. 2017), and purified native CPF contains a mixture of no, one, or two copies of Fip1

(and Pap1). In a recent crystal structure, two hFIP1 molecules are bound to one copy of CPSF30 zinc fingers 4 and 5, with the same region of each hFIP1 bound to each zinc finger (Hamilton and Tong 2020). Notably, the binding affinity of hFIP1 for CPSF30 zinc finger 4 is ~300-fold stronger than for zinc finger 5 (Hamilton and Tong 2020). In agreement, yeast Fip1 also shows a preferential binding toward Yth1 zinc finger 4 and weak interactions with zinc finger 5 (Fig. 1C). Many of the CPSF30 residues involved in binding hFIP1 in the crystal structure undergo changes in our NMR experiments with the yeast proteins, suggesting a similar mode of binding (Fig. 1C). Although we estimate one copy of Fip1 in recombinant CPF based on SEC-MALS, mass photometry, and NMR diffusion experiments, we cannot exclude the possibility that a second Fip1-binding site on Yth1 exists with a much weaker affinity (Supplemental Fig. S5F). It is also possible that Fip1 binding to Yth1 zinc finger 5 is not recapitulated in our recombinant systems. Like most aspects of 3' end processing, the interaction and stoichiometry of Fip1 and Yth1 is likely conserved with that of the human proteins.

#### *Fip1 flexibly tethers Pap1 to CPF and is important for nuclease activation*

The poly(A) polymerase Pap1 was previously known to interact with Fip1 (Preker et al. 1995; Meinke et al. 2008). However, some data had suggested that Pap1 may also contact additional CPF subunits (Murthy and Manley 1995; Ezeokonkwo et al. 2011; Casañal et al. 2017), and it was unclear whether this would be required for stable Pap1 incorporation into CPF. Here, we show that Fip1 is essential for Pap1 association with recombinant CPF, but we did not find any evidence for Pap1 contacting other subunits, at least in the apo complex in the absence of RNA and cleavage factors.

A primary functional role of Fip1 may be to flexibly tether Pap1 to CPF, acting as a nonrigid scaffold for the assembly of a fully functional complex. The binding of Yth1 or Pap1 seems to have minimal effect on the dynamics of the rest of Fip1, including the central LCR. Poly(A) tails are synthesized to a length of ~60 nt in yeast and 150–200 nt in mammals. We hypothesized that a flexible tether would allow Pap1 to follow the growing 3' end of the poly(A) tail until all adenosines have been added, while allowing CPF to remain bound to the polyadenylation signal in the 3' UTR. However, deletion of the central LCR in Fip1 did not substantially affect polyadenylation by CPF. Instead, and surprisingly, it compromised pre-mRNA cleavage (Fig. 6).

Activation of the CPF endonuclease must be highly regulated to prevent spurious cleavage. It is likely that upon RNA binding, conformational changes occur to activate the nuclease and allow RNA to access its active site. Our data suggest that a flexible central LCR is required for efficient nuclease activity, but the LCR sequence is not important. One possibility is that a dynamic Fip1 central LCR is required so that the position of Pap1 within the complex can remain dynamic, preventing steric occlusion of other components (e.g., Ysh1, CF IA, and CF IB). Alter-

natively, the Fip1 central LCR may be required for conformational rearrangements that occur upon pre-mRNA binding and nuclease activation. Since the sequence of the central IDR can be changed with no substantial effect on cleavage activity (Supplemental Fig. S8; Ezeokonkwo et al. 2011), it seems unlikely that it would provide specific binding sites for other proteins; e.g., the accessory cleavage factors that are necessary for efficient nuclease activity.

#### *IDRs are important for CPF function*

Unstructured proteins containing IDRs often bind other proteins to form higher-order complexes and mediate cellular processes (Wright and Dyson 1999; Dyson and Wright 2005). Fip1 is not the only subunit in CPF that contains IDRs. For example, Mpe1, Ref2, Yth1, and Pfs2 also contain regions that are predicted to be disordered (Nedea et al. 2003, 2008; Casañal et al. 2017; Hill et al. 2019). The unstructured N terminus of Yth1 binds to Pfs2 (Casañal et al. 2017), but roles for the other IDRs remain unknown.

One possible function for IDRs within CPF is to mediate flexibility to allow coordination of the four enzymes in CPF, promoting endonuclease activation, endonuclease inactivation, polyadenylation, and transcription termination. Mpe1, a core subunit of the nuclease module, binds directly to Ysh1 and is involved in nuclease activation (Hill et al. 2019; Rodriguez-Molina et al. 2021). Mpe1 contains ordered domains as well as low-complexity regions and is dynamic within a 500-kDa, eight-subunit subcomplex of CPF (Hill et al. 2019). Ref2 is an intrinsically disordered protein that is important for activation of CPF phosphatase activity and transcription termination (Nedea et al. 2008; Choy et al. 2012; Schrieck et al. 2014). IDRs in CPF may allow dynamics and remodeling of CPF.

In this work, we established a recombinant CPF system for the first time. This provides us with the potential to generate variants of CPF components to test additional hypotheses regarding the activation and regulation of the complex. Recombinant CPF was essential for studying the dynamics of Fip1 within CPF, and will allow further studies of the dynamics of single proteins within this large, multiprotein complex. Dynamics within large multiprotein complexes, and specifically IDRs, are difficult to study, especially because characterization of mobile regions is often elusive in cryoEM and X-ray crystallography studies. On the other hand, NMR has an advantage in studying dynamic proteins, but for multiprotein complexes, the large molecular masses and overlapping signals from various components pose a major challenge. Our strategy of using a fully recombinant megadalton CPF with selectively labeled Fip1 ensures the rest of the complex remains NMR-silent, and therefore allows a clean and detailed analysis of a single protein within a large complex. Flexible regions in large complexes can thus produce sharp resonances in NMR spectra, opening up new possibilities to dissect the dynamics and functional roles of IDRs within biological assemblies.

## Materials and methods

### Bioinformatics analysis

Disorder prediction was performed using IUPRED2A in long disorder form (Meszaros et al. 2018). Net charge per residue and fraction of charged residues were calculated using the localCIDER package with a window size of 10 residues (Holehouse et al. 2017). Sequences of homologs of yeast Fip1 were collected from the UniProt database and aligned using ClustalOmega with default parameters (Madeira et al. 2019). The homologs were then divided into N-terminal domain (NTD) and C-terminal domain (CTD) based on the alignment. Residues in the alignment corresponding to yeast Fip1 residues 1–226 were classified as NTD and the rest as CTD. Amino acids were grouped by negatively charged residues (DE), positively charged residues (RK), amines (NQ), small hydrophilic residues (ST), aromatic residues (FYW), aliphatic residues (LVIM), and other small residues (PGA). The frequency of occurrence for each group is defined as the total number of residues in a specific group normalized by the length of each sequence. The occurrence of histidines and cystines are minimal and hence omitted from the plot. Visualizations of data were performed either using custom-written Python or R scripts. Sequence logos were generated using WebLogo (Crooks et al. 2004).

### DNA constructs

Cloning involving pACEBac1, pBIG1, or pBIG2 was performed in DH5 $\alpha$  or TOP10 *E. coli* cells. DH10 EmBacY *E. coli* cells were used to generate and purify all bacmids used in this study. CPF subunit genes were synthesized by GeneArt with their sequences optimized for expression in *E. coli*.

The five-subunit wild-type polymerase module was cloned into the MultiBac protein complex production platform as previously described (Casañal et al. 2017). In brief, Cft1, Pfs2-3C-SII, and 8His-3C-Yth1 were cloned into the pACEBac1 plasmid. The Pfs2 subunit had a C-terminal 3C protease site and a twin StrepII tag (SII). The genes for Pap1 and Fip1 were cloned into the pIDC vector. The five-subunit wild-type polymerase module was generated by Cre-Lox recombination as described (Stowell et al. 2016; Casañal et al. 2017).

Polymerase module truncations and deletions were cloned using a modified version of the biGBac system (Weissmann et al. 2016) as described previously (Hill et al. 2019). Yth1 $_{\Delta ZF45C}$ , Yth1 $_{\Delta ZF5C}$ , Yth1 $_{\Delta ZF4}$ , Fip1 $_{\Delta 1-60}$ , and Fip1 $_{226}$  were amplified by PCR using primers listed in Supplemental Table S1. For deletion of Yth1 zinc finger 4 and Fip1 $_{\Delta 110-180}$ , overlap extension splicing PCR was used. Variants were cloned into pACEBac1 by using BamHI and XbaI restriction sites. The five subunits of the polymerase module were then PCR-amplified from their parent plasmid (pACEBac1 for Cft1, Pfs2-3C-SII, and Yth1, and pIDC plasmid for Pap1 and Fip1) using biGBac primers as described (Weissmann et al. 2016). Each of the five amplified PCR products therefore contains the individual gene with its own promoter and terminator sequences. The five PCR products were cloned into pBIG1a using Gibson assembly to generate a polymerase module containing a Yth1 or Fip1 variant. The final plasmids were verified by SmaI digestion to ensure that the clone contained all five genes in uniform stoichiometry. For the  $\Delta$ Fip1 construct, the Fip1 PCR product was omitted.

For the phosphatase module, Pta1 was cloned into pBIG1a, and Ssu72, Pti1, Glc7, Ref2-3C-SII, and Swd2 were cloned into pBIG1b by Gibson assembly. The Pta1 gene cassette from pBIG1a and the multigene cassette from pBIG1b were released by PmeI digestion. Using a second Gibson assembly step, the PmeI-digest-

ed gene cassettes were introduced into linearized pBIG2ab. Correct insertion of the six phosphatase module genes into pBIG2ab was verified by SmaI and PacI restriction digestion.

The combined nuclease and phosphatase module (“CPFcore”) was assembled without any affinity tags in this work. First, the five-subunit polymerase module (Cft1, Pap1, Pfs2, Fip1, and Yth1) was cloned into pBIG1a and a three-subunit nuclease module (Cft2, Ysh1, and Mpe1) was cloned into pBIG1b with Gibson assembly. The multigene cassettes from pBIG1a and pBIG1b were cut by PmeI restriction digestion and cloned into pBIG2ab. For CPF $\Delta$ Fip1, Fip1 was omitted from the CPFcore construct. For Fip1 $_{\Delta 110-180}$ , the Fip1 variant was used.

CFIA subunits Rna14, Rna15, Pcf11, and Clp1 were cloned into the pBIG1c vector using Gibson assembly as described above for the polymerase module subunits.

The sequence corresponding to Fip1 residues 1–226 was cloned into pET28a+ using PCR with primers listed in Supplemental Table S1 and NdeI and HindIII restriction sites. The sequence corresponding to Yth1 zinc finger 4 (residues 108–161) or Yth1 zinc fingers 4 and 5 and the rest of the C-terminal region (residues 118–208) was cloned into pGEX6P-2 using PCR with primers listed in Supplemental Table S1 and BamHI and EcoRI restriction sites.

### Baculovirus-mediated protein overexpression

Plasmids encoding the protein or protein complex of interest were transformed into *E. coli* DH10 EmBacY cells. Colonies that had successfully integrated the plasmid into the baculovirus genome were picked using blue/white selection methods. A 5-mL overnight culture of the selected colony was set up in 2 $\times$  TY media. For pACEBac1 and pBIG1 vectors, 10  $\mu$ g/mL gentamycin was used. For pBIG2 vectors, both 10  $\mu$ g/mL gentamycin and 35  $\mu$ g/mL chloramphenicol were used. Bacmids were purified from these cultures using protocols described earlier (Stowell et al. 2016).

A total of 10  $\mu$ g of bacmid DNA was transfected into six wells of 2 $\times$  10<sup>6</sup> adherent Sf9 cells (at 5 $\times$  10<sup>5</sup> cells/mL) using the transfection reagent Fugene HD (Promega). Forty-two hours to 72 h after transfection, the viral supernatant was isolated, diluted twofold with sterile FBS (Labtech), and filtered through a 0.45- $\mu$ m sterile filter (Millipore). This primary virus could be stored in the dark for up to 1 yr at 4°C. We then used 0.5 mL of the primary virus to infect 50 mL of Sf9 cells in suspension at  $\sim$ 2 $\times$  10<sup>6</sup> cells/mL. The infection was monitored every 24 h by taking note of the cell viability, cell count, and YFP fluorescence. Forty-eight hours to 72 h after infection, the cells usually undergo growth arrest. During this time, robust fluorescence indicating high levels of protein expression can be observed. The supernatant from this suspension culture was harvested by centrifugation at 2000g for 10 min. The resulting supernatant or “secondary virus” was filtered using 0.45- $\mu$ m pore size sterile filter (Millipore) and was used immediately to infect large-scale expression cultures. For large-scale protein expression, 5 mL of secondary virus was used to infect 500-mL suspension Sf9 cells (at 2 $\times$  10<sup>6</sup> cells/mL and viability >90%) grown in a 2-L roller bottle flask. All Sf9 cells were grown in insect-Express (Lonza) media, incubated at 140 rpm and 27°C. No additional supplements were provided to the media.

For the production of a recombinant 14-subunit CPF, the following modifications were made. Five milliliters of primary virus was used to infect 100 mL of Sf9 cells (at 2 $\times$  10<sup>6</sup> cells/mL) grown in suspension in a 500-mL Erlenmeyer flask. Forty-eight hours to 72 h after infection, when the cell count was  $\sim$ 3 $\times$  10<sup>6</sup> cells/mL (>90% viability) and  $\sim$ 80% of the cells exhibited YFP fluorescence, the supernatant or the secondary virus was harvested. For large-scale overexpression, 5 mL of the phosphatase module secondary virus along with 5 mL of the CPFcore (combined nuclease and polymerase modules) secondary virus were used to infect 500 mL of Sf9

cells (at  $2 \times 10^6$  cells/mL) grown in suspension in a 2-L roller bottle flask. The cells were harvested either at 48 or 72 h after infection. The exact time of harvest was decided by performing small-scale protein pull-downs as described in the next section. Upon harvesting, the cell pellets were washed once with prechilled PBS, flash-frozen in liquid nitrogen, and stored at  $-80^\circ\text{C}$ .

#### Small-scale pull-down assays

Small-scale pull-down assays were used to assess protein expression. We used 0.5 mL secondary virus to infect 50 mL of *Sf9* cells ( $2 \times 10^6$  cells/mL, viability  $>90\%$ ) in a 200-mL Erlenmeyer flask. For 96 h after infection,  $\sim 10^7$  cells were harvested at 24-h time points by centrifugation at 2000g for 10 min. Cells were flash-frozen in liquid nitrogen and stored at  $-20^\circ\text{C}$ . All subsequent steps were performed at  $4^\circ\text{C}$  unless otherwise stated. First, the pellets were lysed in 1 mL of pull-down lysis buffer and lysed using vortexing for 2 min with glass beads in a 1.5-mL tube. The lysate was clarified by centrifugation for 30 min in a tabletop centrifuge at maximum speed. The supernatant was incubated for 2 h with 20  $\mu\text{L}$  of Strep-tactin resin (GE) that had been washed and pre-equilibrated in pull-down lysis buffer. Protein binding was carried out with mixing for 2 h. Unbound proteins were separated from the resin by centrifugation at 600g for 10 min. The resin was then washed twice with 1 mL of pull-down wash buffer. The bound proteins were eluted with 20  $\mu\text{L}$  of pull-down elution buffer for 5 min. The elution fraction was recovered by centrifugation at 600g for 10 min. Twelve microliters of eluted proteins was mixed with 4  $\mu\text{L}$  of 4 $\times$  NuPAGE LDS sample buffer (Thermo Fisher) and analyzed by SDS-PAGE (4%–12% Bis-Tris gradient gel [Thermo Fisher] with MOPS running buffer, run at 180 V for 60 min at room temperature).

#### Purification of recombinant CPF complexes

The wild-type five-subunit polymerase module was expressed and purified as previously described (Casañal et al. 2017). Buffers for CPF purifications are listed in Supplemental Table S2. All steps were performed at  $4^\circ\text{C}$  unless otherwise stated and the following amounts are given for a preparation from 2 L of cells. Frozen *Sf9* cells pellets were resuspended in 120 mL of CPF lysis buffer. The cells were lysed by sonication using a 10-mm tip on a VC 750 ultrasonic processor (Sonics). Sonication was performed at 70% amplitude with 5 sec on and 10 sec off. The lysate was clarified by ultracentrifugation at 18,000 rpm in a JA 25.50 rotor for 30 min. The clarified lysate was incubated with 2 mL of bed volume StrepTactin Sepharose HP resin (GE) that was pre-equilibrated with CPF lysis buffer. Protein was allowed to bind for 2 h in an end-over-end rotor. The unbound proteins were separated from the resin by centrifugation at 600g for 10 min. The resin was then washed in a gravity column with 200 mL of CPF wash buffer. Elution was performed at room temperature with 10 fractions, each with 3 mL of ice-chilled CPF elution buffer incubated for 5–10 min on the gravity column. The eluted fractions were pooled and loaded on to a 1-mL resource Q anion exchange column (GE) that was equilibrated with CPF wash buffer. CPF was eluted from the resource Q column using a gradient from 0.15 to 1 M KCl over 100 mL. The eluted fractions were assessed by SDS-PAGE. Such a shallow gradient elution across 100 mL aided in the complete separation of the 14-subunit CPF complex from subcomplexes. Next, CPF-containing fractions with stoichiometric subunit amounts were pooled and concentrated in a 50-kDa Amicon centrifugal filter (Sigma) at 4000 rpm in a tabletop centrifuge. Fifty microliters of concentrated CPF sample was polished further by gel filtration chromatography using a Superose 6 Increase 3.2/300 column (GE) with CPF wash buffer at a flow rate of 0.06

mL/min. The peak fractions from the size exclusion step were analyzed by SDS-PAGE. The fractions were concentrated, flash-frozen in liquid nitrogen, and stored at  $-80^\circ\text{C}$ . For biochemical assays, pure CPF-containing fractions were used immediately after the anion exchange purification step.

Recombinant CPF containing Fip1 central LCR variants (Fip1<sub>scramble</sub> or Fip1<sub>Puf3</sub>) were prepared by coinfecting *Sf9* cells in suspension at  $\sim 2 \times 10^6$  cells/mL with the secondary viruses of the Fip1 variants, and a secondary virus of the Cft1, Pfs2-SII, and Yth1 complex in a 1:1 ratio (by volume). The resulting four-protein polymerase module was purified using the same protocol as wild-type polymerase module. The enzyme Pap1 was purified from *E. coli* (see details below). The nine-subunit complex of the combined nuclease and phosphatase modules was expressed by coinfecting *Sf9* cells in suspension at  $\sim 2 \times 10^6$  cells/mL with a secondary virus of the nuclease module, and a secondary virus of the phosphatase module. The complex of the combined nuclease and phosphatase modules was purified following the same procedure described for recombinant CPF complexes. Finally, full CPF containing each of the Fip1 variants was assembled by mixing the three purified protein complexes (Pap1, Cft1-Pfs2-SII-Yth1-Fip1, and the nuclease-phosphatase module) and performing size exclusion chromatography using a Superose 6 Increase 3.2/300 column (GE) with CPF wash buffer. Fractions containing all subunits of CPF were pooled and concentrated using a 100-kDa Amicon centrifugal filter (Sigma) at 10,000 rpm in a tabletop centrifuge. In Fip1<sub>scramble</sub>, Fip1 residues 110–170 were replaced by NTTDALSGAIGNPIMRTAVSTTVVDESTGLADGEVTKESDDKDIVIGTQKSTVEAKSKENT. In Fip1<sub>Puf3</sub>, Fip1 residues 110–170 were replaced by *S. pombe* Puf3 residues 3–63 TAVNSNPNAS ESISGNSAFNFPSPVSSLDNTNNGYQRRPSSLGTSPTSSFFNS SMISSNY.

#### Purification of cleavage factors

CF IB was purified as described previously (Hill et al. 2019). Purification of CF IA was carried out essentially as described for recombinant CPF with the corresponding buffers listed in Supplemental Table S2, and with the following modifications. Pooled eluate fractions from StrepTactin Sepharose HP resin was applied to a 5-mL HiTrap Heparin HP (GE) column equilibrated in CF IA wash buffer, and subsequently eluted using a linear 0.25–1 M NaCl gradient over 100 mL. Following SDS-PAGE analysis and concentration of pooled fractions, CF IA was further purified by gel filtration using a HiLoad 26/60 Superdex 200-pg column in CF IA wash buffer. The peak fractions were assessed by SDS-PAGE for sample purity. During concentration of the pooled fractions showing correct complex stoichiometry, care was taken not to overconcentrate the sample (maximum 7 mg/mL). The concentrated purified protein complex was flash-frozen in liquid nitrogen and stored at  $-80^\circ\text{C}$  until further use.

#### Protein expression and purification in *E. coli*

Buffers for purifications are listed in Supplemental Table S2. Yth1 proteins were expressed in BL21 Star with an N-terminal GST tag. Isotopically labeled proteins were overexpressed in M9 media (6 g/L  $\text{Na}_2\text{HPO}_4$ , 3 g/L  $\text{KH}_2\text{PO}_4$ , 0.5 g/L NaCl) supplemented with 1.7 g/L yeast nitrogen base without  $\text{NH}_4\text{Cl}$  and amino acids (Sigma Y1251). We supplemented 1 g/L  $^{15}\text{NH}_4\text{Cl}$  and 4 g/L  $^{13}\text{C}$ -glucose for  $^{15}\text{N}$  and  $^{13}\text{C}$  labelling, respectively. Expression was induced with 1 mM IPTG for 16 h at  $22^\circ\text{C}$ . Harvested cells were lysed by sonication in buffer A supplemented with 2  $\mu\text{g}/\text{mL}$  DNase I, 2  $\mu\text{g}/\text{mL}$  RNase A, and protease inhibitor mixture (Roche). Proteins were bound to GST resin (GE Healthcare) and

eluted in buffer A supplemented with 10 mM glutathione (pH-calibrated). Eluted protein was subjected to 3C protease cleavage and loaded onto a Superdex 75 size exclusion column pre-equilibrated with buffer A. Fractions containing Yth1 were pooled and concentrated using 3000 MWCO concentrators (Millipore).

Fip1<sub>226</sub> was expressed in BL21 Star with an N-terminal His tag. Isotopically labeled proteins were overexpressed as described for Yth1 constructs. Perdeuterated proteins were overexpressed in cells with step adaptations in media with 10%, 44%, and 78% D<sub>2</sub>O, before switching to 100% perdeuterated media supplemented with 1 g/L <sup>15</sup>NH<sub>4</sub>Cl and 4 g/L <sup>2</sup>H, <sup>13</sup>C-glucose. Harvested cells were lysed by sonication in buffer B supplemented with 2 µg/mL DNase I, 2 µg/mL RNase A, and protease inhibitor mixture (Roche). Proteins were bound to Ni-NTA resin (GE Healthcare) and eluted with buffer B with 250 mM imidazole (pH-calibrated). Eluted protein was subjected to TEV protease cleavage and loaded onto a Superdex 75 size exclusion column pre-equilibrated with buffer A used for Yth1 constructs. Fractions containing Fip1<sub>226</sub> were pooled and concentrated using 10,000 MWCO concentrators (Millipore).

Pap1 was expressed in BL21 Star as an N-terminal His-tagged protein. Expression was induced with 1 mM IPTG for 16 h at 22°C. Harvested cells were lysed by sonication in Pap1 lysis buffer. Proteins were bound to Ni-NTA resin (GE Healthcare) and eluted in 50 mM HEPES (pH 8.0), 500 mM NaCl, and 300 mM imidazole. Eluted protein was exchanged into buffer containing 50 mM HEPES (pH 8.0), 100 mM NaCl, and 0.5 mM TCEP; loaded onto a HiTrap Heparin column (GE Healthcare); and eluted with Pap1 buffer. Eluted protein was pooled and loaded onto a Superdex 200 size exclusion column pre-equilibrated with Pap1 SEC buffer. Fractions containing His-Pap1 were pooled and concentrated using 30,000 MWCO concentrators (Millipore).

#### CryoEM of polymerase module

UltraAufoil R1.2/1.3 gold supports (Russo and Passmore 2014) were used to make grids of freshly purified polymerase module containing Pap1. Three microliters of purified protein complex was applied onto glow-discharged gold grids in an FEI Vitrobot MKIII chamber maintained at 100% humidity and 4°C followed by 3-sec blot (Whatman filter paper) with a blot force of -10 and vitrification in liquid ethane.

Samples were imaged on a FEI Titan Krios operated at 300 keV and equipped with a Falcon-II direct electron detector. A total of 852 micrographs was acquired at a magnification of 47,000× (corresponding to a calibrated pixel size of 1.77 Å) in linear mode. The total electron dose was ~35 e-/Å<sup>2</sup>. The frames were aligned and averaged with MotionCorr (Li et al. 2013) and CTF estimation was performed using Gctf embedded in Relion-2 (Kimanius et al. 2016; Zhang 2016). In total, 628 micrographs were selected for further data analysis. Approximately 4000 particles were manually picked using a mask diameter of 200 Å and a box size of 140 pixels. 2D classes obtained from these manually picked particles were then used as templates for autopicking in Relion (picking threshold 0.5, minimum interparticle distance 100 Å). A total of 216,375 particles was extracted with a box size of 160 pixels and subjected to 2D classification. Further 3D classification and refinement led to a map that was highly similar to our previously determined cryoEM map of Cft1-Pfs2-Yth1 subunits with no additional density that could correspond to Pap1.

#### Isothermal titration calorimetry (ITC)

Samples were prepared in 50 mM HEPES (pH 7.4) and 150 mM NaCl. ITC measurements were performed using a MicroCal ITC200 (Malvern) with Yth1<sub>ZF4</sub> and Fip1<sub>226</sub>. Protein concentra-

tions are listed in the figure legends. The experiments were conducted at 25°C with 14 injections of 2.6 µL preceded by a small 0.5-µL preinjection that was not included during fitting. For data analysis, appropriate control heats of dilution of protein injected into buffer was subtracted from the raw data and the result was fitted using a single class-binding site model in the manufacturer's PEAQ software to determine the affinity and stoichiometry of binding.

#### SEC-MALS

Recombinant CPF was analyzed using a Heleos II 18-angle light scattering instrument (Wyatt Technology) and Optilab rEX online refractive index detector (Wyatt Technology) at room temperature. One-hundred microliters of purified recombinant CPF at 1 mg/mL was loaded onto a Superdex 200 10/300 GL increase column (GE Healthcare) pre-equilibrated with 50 mM HEPES (pH 7.4) and 150 mM NaCl, running at 0.5 mL/min. The molecular mass was determined from the intercept of the Debye plot using the Zimm model as implemented in Astra software (Wyatt Technology). Protein concentration was determined from the excess differential refractive index based on a 0.186 refractive index increment for 1 g/mL protein solution.

#### Mass photometry/interferometric scattering microscopy

Measurements were performed with the Refeyn One iSCAT instrument using coverslips and sample gaskets carefully cleaned with isopropanol. Samples were diluted in 50 mM HEPES (pH 7.4) and 150 mM NaCl buffer to 100 nM, and 10 µL was loaded into the gasket well. Data were collected for 1 min at 100 Hz and the resultant movies were analyzed using ratiometric averaging of five frame bins. Mass was obtained from ratiometric contrast using a standard curve obtained for proteins of known mass measured on the instrument. This technique has been reported to measure molecular mass up to a precision of 1.8% ± 0.5% (Young et al. 2018).

#### In vitro pull-down assays

Bait proteins and complexes containing a StrepII tag were diluted to a concentration of 1.5 µM in 50 mM HEPES (pH 7.4) and 150 mM NaCl. One-hundred microliters of bait protein was mixed with 40 µL of bed volume StrepTactin resin (GE Healthcare) and incubated for 1 h at 4°C. Resins were washed with loading buffer three times and eluted with 6 mM desthiobiotin. Elution was analyzed with a 4%–12% gradient SDS gel.

#### In vitro cleavage and polyadenylation assays

Polyadenylation assays were used to test the functional activity of the polymerase module and its variants, and CPF. A 42-nt pre-cleaved *CYC1* (pc*CYC1*) RNA with a 5' 6-FAM fluorophore (IDT) was used as a substrate for polyadenylation assays as previously described (Casañal et al. 2017).

For coupled assays, the 56-nt *CYC1* RNA substrate contained a 5' 6-FAM fluorophore (IDT) and a 3' AlexaFluor 647 (IDT) as in Hill et al. (2019). For cleavage-only assays, a similar 36-nt *CYC1c* RNA substrate was used (Hill et al. 2019). Reactions contained 100 nM *CYC1* RNA substrate, 50 nM recombinant CPF or its variants, and 300 nM CF IA and CF IB. The reactions were carried out in 10 mM HEPES (pH 7.9), 150 mM KOAc, 2 mM Mg (OAc)<sub>2</sub>, 0.05 mM EDTA, and 2% (v/v) PEG with 1 mM DTT and 1 U/µL RiboLock (Thermo) at 30°C. The reaction products were analyzed by denaturing 20% acrylamide/7 M urea PAGE

to resolve the cleavage products and 10% acrylamide/7 M urea PAGE to visualize the polyadenylation bands. The gels were preheated at 30 W for 30 min prior to loading the samples and running for 10–20 min at 400 V. The gels were then scanned on a Typhoon FLA-7000 (GE) using the 473-nm laser/Y520 filter for FAM and the 635-nm laser/R670 filter for AlexaFluor647.

#### NMR spectroscopy

Most experiments on Yth1 and Fip1<sub>226</sub> were performed using in-house Bruker 700-MHz Avance II+ and 800-MHz Avance III spectrometers, both equipped with a triple-resonance TCI CryoProbe. For some samples (as indicated below), we also used the Bruker 950-MHz Avance III spectrometer located at MRC Biomedical NMR Centre.

All experimental data on Yth1 constructs were collected at 700 MHz in 50 mM HEPES (pH 7.4) and 150 mM NaCl. <sup>15</sup>N-labeled proteins were used for binding studies, and <sup>13</sup>C, <sup>15</sup>N-labeled proteins were used for backbone assignment. Backbone experiments and relaxation experiments were acquired at 278 K to extend sample lifetimes, and binding experiments were acquired at 298 K to overcome exchange broadening. The dependency of individual peaks was studied by increasing the temperature in 5-K steps.

Experimental data on Fip1<sub>226</sub> were collected at 700, 800, and 950 MHz. All experiments on Fip1<sub>226</sub> were carried out at 278 K. Backbone experiments were acquired using <sup>2</sup>H, <sup>13</sup>C, <sup>15</sup>N-labeled samples at 800 MHz and 950 MHz in 50 mM HEPES (pH 7.4) and 50 mM NaCl to recover most signals from exchange broadening. <sup>13</sup>C-detect experiments were acquired at 700 MHz. Binding studies, unless otherwise specified, were carried out at 800 MHz in 50 mM HEPES (pH 7.4) and 150 mM NaCl.

To prepare CPF for NMR, isotopically labeled Fip1<sub>226</sub> was mixed with 1.1-fold molar excess of CPFΔFip1. The complex was buffer-exchanged into 50 mM HEPES (pH 7.4) and 150 mM NaCl. His-Pap1 used for binding studies was exchanged into the same buffer before being added to the CPF-Fip1<sub>226</sub> samples. Experimental data on CPF-Fip1<sub>226</sub> were collected at 950 MHz. All experiments were carried out at 278 K in 50 mM HEPES (pH 7.4) and 150 mM NaCl. Five percent D<sub>2</sub>O and 0.05% sodium azide (final concentration) were added to the samples before NMR analysis.

#### Backbone assignment

Assignment of backbone amide peaks of Yth1 constructs was carried out using the following standard triple-resonance spectra: HNCO, HN(CA)CO, HNCA, HNCACB, HN(CO)CACB, HN(CAN)NH, and HN(COCA)NNH (Bruker). TROSY versions of these spectra were used for the backbone assignment of Fip1<sub>226</sub>. Backbone data sets were collected with nonuniform sampling at 20%–50% and processed with compressed sensing using MddNMR package (Jaravine et al. 2008). Resonances from proline residues in Fip1<sub>226</sub> were assigned using <sup>1</sup>H start versions of <sup>13</sup>C-detect CON, H(CA)CON, and H(CA)NCO (Bruker). Backbone resonances were assigned manually with the aid of Mars (Jung and Zweckstetter 2004). Topspin 3.6 (Bruker) was used for processing and NMRFAM-Sparky 1.47 (Lee et al. 2015) was used for spectra analysis.

#### Secondary chemical shifts

Cα/Cβ chemical shift deviations were calculated using the equation (δCα<sub>obs</sub> – δCα<sub>rc</sub>) – (δCβ<sub>obs</sub> – δCβ<sub>rc</sub>), where δCα<sub>obs</sub> and δCβ<sub>obs</sub> are the observed Cα and Cβ chemical shifts and δCα<sub>rc</sub> and δCβ<sub>rc</sub> are the Cα and Cβ chemical shifts for random coils (Kjaergaard and Poulsen 2011). Temperature coefficients (Kjaergaard et al.

2011) and correction factors for perdeuteration (Maltsev et al. 2012) were applied to the random coil chemical shifts where applicable.

#### Binding studies

Weighted chemical shift perturbations were calculated using the equation (Ayed et al. 2001)

$$\Delta\delta = [(\Delta\delta_{\text{HN}}W_{\text{HN}})^2 + (\Delta\delta_{\text{N}}W_{\text{N}})^2 + (\Delta\delta_{\text{CO}}W_{\text{CO}})^2]^{1/2},$$

with weight factors determined from the average variances of chemical shifts in the BioMagResBank chemical shift database (Mulder et al. 1999), where  $W_{\text{HN}} = 1$ ,  $W_{\text{N}} = 0.16$ , and  $W_{\text{CO}} = 0.34$ .

#### Relaxation measurements

<sup>15</sup>N T2 relaxation times were measured using standard INEPT-based 3D pulse sequences (Bruker) at a spin lock field of 500 Hz and initial delay of 5 sec. Twelve mixing times were collected (8.48, 16.96, 33.92, 50.88, 67.84, 101.76, 135.68, 169.6, 203.52, 237.44, 271.36, and 8.48 msec) and peak height analysis was done in NMRFAM-Sparky 1.47 (Lee et al. 2015). <sup>15</sup>N{<sup>1</sup>H}-hetNOE measurements were carried out using standard Bruker pulse programs, with interleaved on-resonance (I) or off-resonance (I<sub>0</sub>) saturation. The hetNOE values were analyzed in NMRFAM-Sparky 1.47 taking I/I<sub>0</sub>. The hetNOE values were obtained by averaging two experiments. The reported error values are calculated standard deviations.

#### Diffusion experiments

An <sup>15</sup>N-edited <sup>1</sup>H XSTE diffusion experiment with watergate (Ferrage et al. 2003) was used to measure diffusion coefficients of <sup>15</sup>N-labeled species in the sample using a diffusion delay of 100 msec and a 4-msec gradient pulse pair for encoding and decoding, respectively. Peak intensities at two gradient strengths (5% and 95%) were integrated and the diffusion coefficient was calculated using Stejskal-Tanner equation, where  $I$  is peak intensity,  $G$  is gradient strength,  $\delta$  is length of gradient pulse pair,  $\gamma$  is <sup>1</sup>H gyromagnetic ratio, and  $\Delta$  is diffusion delays:

$$I_f = I_0 e^{-G^2 \delta^2 \gamma^2 [\Delta - (\delta/3) - \tau/2] D}.$$

Hydrodynamic radius was deduced using the Stokes-Einstein equation  $R_h = kT / (6\pi\eta D)$ , where  $k$  is the Boltzmann constant,  $T$  is absolute temperature, and  $\eta$  is solvent viscosity. The hydrodynamic radius was converted to the effective molecular mass using the equation  $R_h = 0.066 M^{1/3}$  (Erickson 2009).

#### Data availability

NMR data sets have been deposited in BMRB with accession codes 50795 (Fip1<sub>226</sub>), 50796 (Yth1<sub>ZF4</sub>), and 50797 (Yth1<sub>ZF45C</sub>).

#### Competing interest statement

The authors declare no competing interests.

#### Acknowledgments

We thank Chris Johnson (MRC Laboratory of Molecular Biology) for help with biophysics, M. Cemre Manav (MRC Laboratory of Molecular Biology) for purified CPF modules, Chris Hill (MRC

Laboratory of Molecular Biology) for CF IA plasmids, and members of the Passmore laboratory for assistance and advice. This work was supported by a Gates Cambridge PhD Studentship (to A.K.), the European Union's Horizon 2020 research and innovation program (ERC grant 725685 to L.A.P.), Marie Skłodowska-Curie (grant 838945 to X.-H.L.), and the Medical Research Council, as part of United Kingdom Research and Innovation (MRC grant MC\_U105192715 to L.A.P.). Some of the NMR studies were supported by the Francis Crick Institute through access to the MRC Biomedical NMR Centre. The Francis Crick Institute receives its core funding from Cancer Research UK (FC001029), the UK Medical Research Council (FC001029), and the Wellcome Trust (FC001029).

*Author contributions:* A.K., C.W.H.Y., and L.A.P. conceived the study. A.K., C.W.H.Y., and J.B.R.-M. purified proteins and performed assays. C.W.H.Y. performed biophysical studies. C.W.H.Y. and S.M.V.F. performed NMR studies. X.-H.L. performed bioinformatic analyses. A.K., C.W.H.Y., and L.A.P. wrote the manuscript. All authors discussed and commented on the final manuscript.

## References

- Ayed A, Mulder FA, Yi GS, Lu Y, Kay LE, Arrowsmith CH. 2001. Latent and active p53 are identical in conformation. *Nat Struct Biol* **8**: 756–760. doi:10.1038/nsb0901-756
- Balbo PB, Bohm A. 2007. Mechanism of poly(A) polymerase: structure of the enzyme-MgATP-RNA ternary complex and kinetic analysis. *Structure* **15**: 1117–1131. doi:10.1016/j.str.2007.07.010
- Barabino SM, Ohnacker M, Keller W. 2000. Distinct roles of two Yth1p domains in 3'-end cleavage and polyadenylation of yeast pre-mRNAs. *EMBO J* **19**: 3778–3787. doi:10.1093/emboj/19.14.3778
- Bard J, Zhelkovsky AM, Helmling S, Earnest TN, Moore CL, Bohm A. 2000. Structure of yeast poly(A) polymerase alone and in complex with 3'-dATP. *Science* **289**: 1346–1349. doi:10.1126/science.289.5483.1346
- Casañal A, Kumar A, Hill CH, Easter AD, Emsley P, Degliesposti G, Gordiyenko Y, Santhanam B, Wolf J, Wiederhold K, et al. 2017. Architecture of eukaryotic mRNA 3'-end processing machinery. *Science* **358**: 1056–1059. doi:10.1126/science.aao6535
- Choy MS, Page R, Peti W. 2012. Regulation of protein phosphatase 1 by intrinsically disordered proteins. *Biochem Soc Trans* **40**: 969–974. doi:10.1042/BST20120094
- Clerici M, Faini M, Aebersold R, Jinek M. 2017. Structural insights into the assembly and polyA signal recognition mechanism of the human CPSF complex. *Elife* **6**: e33111. doi:10.7554/eLife.33111
- Clerici M, Faini M, Muckenfuss LM, Aebersold R, Jinek M. 2018. Structural basis of AAUAAA polyadenylation signal recognition by the human CPSF complex. *Nat Struct Mol Biol* **25**: 135–138. doi:10.1038/s41594-017-0020-6
- Crooks GE, Hon G, Chandonia JM, Brenner SE. 2004. WebLogo: a sequence logo generator. *Genome Res* **14**: 1188–1190. doi:10.1101/gr.849004
- Curinha A, Oliveira Braz S, Pereira-Castro I, Cruz A, Moreira A. 2014. Implications of polyadenylation in health and disease. *Nucleus* **5**: 508–519. doi:10.4161/nucl.36360
- Dyson HJ, Wright PE. 2005. Intrinsically unstructured proteins and their functions. *Nat Rev Mol Cell Biol* **6**: 197–208. doi:10.1038/nrm1589
- Erickson HP. 2009. Size and shape of protein molecules at the nanometer level determined by sedimentation, gel filtration, and electron microscopy. *Biol Proced Online* **11**: 32–51. doi:10.1007/s12575-009-9008-x
- Ezeokonkwo C, Zhelkovsky A, Lee R, Bohm A, Moore CL. 2011. A flexible linker region in Fip1 is needed for efficient mRNA polyadenylation. *RNA* **17**: 652–664. doi:10.1261/rna.2273111
- Ferrage F, Zoonens M, Warschawski DE, Popot JL, Bodenhausen G. 2003. Slow diffusion of macromolecular assemblies by a new pulsed field gradient NMR method. *J Am Chem Soc* **125**: 2541–2545. doi:10.1021/ja0211407
- Fuxreiter M, Tóth-Petróczy A, Kraut DA, Matouschek A, Lim RY, Xue B, Kurgan L, Uversky VN. 2014. Disordered protein-aceous machines. *Chem Rev* **114**: 6806–6843. doi:10.1021/cr4007329
- Ghazy MA, He X, Singh BN, Hampsey M, Moore C. 2009. The essential N terminus of the Pta1 scaffold protein is required for snoRNA transcription termination and Ssu72 function but is dispensable for pre-mRNA 3'-end processing. *Mol Cell Biol* **29**: 2296–2307. doi:10.1128/MCB.01514-08
- Hamilton K, Tong L. 2020. Molecular mechanism for the interaction between human CPSF30 and hFip1. *Genes Dev* **34**: 1753–1761. doi:10.1101/gad.343814.120
- Helmling S, Zhelkovsky A, Moore CL. 2001. Fip1 regulates the activity of Poly(A) polymerase through multiple interactions. *Mol Cell Biol* **21**: 2026–2037. doi:10.1128/MCB.21.6.2026-2037.2001
- Hill CH, Boreikaitė V, Kumar A, Casañal A, Kubík P, Degliesposti G, Maslen S, Mariani A, von Loeffelholz O, Girbig M, et al. 2019. Activation of the endonuclease that defines mRNA 3' ends requires incorporation into an 8-subunit core cleavage and polyadenylation factor complex. *Mol Cell* **73**: 1217–1231.e11. doi:10.1016/j.molcel.2018.12.023
- Hocine S, Singer RH, Grunwald D. 2010. RNA processing and export. *Cold Spring Harb Perspect Biol* **2**: a000752. doi:10.1101/cshperspect.a000752
- Holehouse AS, Das RK, Ahad JN, Richardson MO, Pappu RV. 2017. CIDER: resources to analyze sequence-ensemble relationships of intrinsically disordered proteins. *Biophys J* **112**: 16–21. doi:10.1016/j.bpj.2016.11.3200
- Jaravine VA, Zhuravleva AV, Permi P, Ibraghimov I, Orekhov VY. 2008. Hyperdimensional NMR spectroscopy with nonlinear sampling. *J Am Chem Soc* **130**: 3927–3936. doi:10.1021/ja077282o
- Jung YS, Zweckstetter M. 2004. Mars—robust automatic backbone assignment of proteins. *J Biomol NMR* **30**: 11–23. doi:10.1023/B:JNMR.0000042954.99056.ad
- Kaufmann I, Martin G, Friedlein A, Langen H, Keller W. 2004. Human Fip1 is a subunit of CPSF that binds to U-rich RNA elements and stimulates poly(A) polymerase. *EMBO J* **23**: 616–626. doi:10.1038/sj.emboj.7600070
- Kimanius D, Forsberg BO, Scheres SH, Lindahl E. 2016. Accelerated cryo-EM structure determination with parallelisation using GPUs in RELION-2. *Elife* **5**: e18722. doi:10.7554/eLife.18722
- Kjaergaard M, Poulsen FM. 2011. Sequence correction of random coil chemical shifts: correlation between neighbor correction factors and changes in the ramachandran distribution. *J Biomol NMR* **50**: 157–165. doi:10.1007/s10858-011-9508-2
- Kjaergaard M, Brander S, Poulsen FM. 2011. Random coil chemical shift for intrinsically disordered proteins: effects of temperature and pH. *J Biomol NMR* **49**: 139–149. doi:10.1007/s10858-011-9472-x
- Kumar A, Clerici M, Muckenfuss LM, Passmore LA, Jinek M. 2019. Mechanistic insights into mRNA 3'-end processing.



- Curr Opin Struct Biol* **59**: 143–150. doi:10.1016/j.sbi.2019.08.001
- Lee W, Tonelli M, Markley JL. 2015. NMRFAM-SPARKY: enhanced software for biomolecular NMR spectroscopy. *Bioinformatics* **31**: 1325–1327. doi:10.1093/bioinformatics/btu830
- Li X, Mooney P, Zheng S, Booth CR, Braumfeld MB, Gubbens S, Agard DA, Cheng Y. 2013. Electron counting and beam-induced motion correction enable near-atomic-resolution single-particle cryo-EM. *Nat Methods* **10**: 584–590. doi:10.1038/nmeth.2472
- Madeira F, Park YM, Lee J, Buso N, Gur T, Madhusoodanan N, Basutkar P, Tivey ARN, Potter SC, Finn RD, et al. 2019. The EMBL-EBI search and sequence analysis tools APIs in 2019. *Nucleic Acids Res* **47**: W636–W641. doi:10.1093/nar/gkz268
- Maltsev AS, Ying J, Bax A. 2012. Deuterium isotope shifts for backbone  $^1\text{H}$ ,  $^{15}\text{N}$  and  $^{13}\text{C}$  nuclei in intrinsically disordered protein  $\alpha$ -synuclein. *J Biomol NMR* **54**: 181–191. doi:10.1007/s10858-012-9666-x
- Meinke G, Ezeokonkwo C, Balbo P, Stafford W, Moore C, Bohm A. 2008. Structure of yeast poly(A) polymerase in complex with a peptide from Fip1, an intrinsically disordered protein. *Biochemistry* **47**: 6859–6869. doi:10.1021/bi800204k
- Meszáros B, Erdos G, Dosztanyi Z. 2018. IUPred2a: context-dependent prediction of protein disorder as a function of redox state and protein binding. *Nucleic Acids Res* **46**: W329–W337. doi:10.1093/nar/gky384
- Mulder FA, Schipper D, Bott R, Boelens R. 1999. Altered flexibility in the substrate-binding site of related native and engineered high-alkaline *Bacillus subtilis*ins. *J Mol Biol* **292**: 111–123. doi:10.1006/jmbi.1999.3034
- Murthy KG, Manley JL. 1995. The 160-kD subunit of human cleavage-polyadenylation specificity factor coordinates pre-mRNA 3'-end formation. *Genes Dev* **9**: 2672–2683. doi:10.1101/gad.9.21.2672
- Nedea E, He X, Kim M, Pootoolal J, Zhong G, Canadien V, Hughes T, Buratowski S, Moore CL, Greenblatt J. 2003. Organization and function of APT, a subcomplex of the yeast cleavage and polyadenylation factor involved in the formation of mRNA and small nucleolar RNA 3'-ends. *J Biol Chem* **278**: 33000–33010. doi:10.1074/jbc.M304454200
- Nedea E, Nalbant D, Xia D, Theoharis NT, Suter B, Richardson CJ, Tatchell K, Kislinger T, Greenblatt JF, Nagy PL. 2008. The Glc7 phosphatase subunit of the cleavage and polyadenylation factor is essential for transcription termination on snoRNA genes. *Mol Cell* **29**: 577–587. doi:10.1016/j.molcel.2007.12.031
- Ohnacker M, Barabino SM, Preker PJ, Keller W. 2000. The WD-repeat protein pfs2p bridges two essential factors within the yeast pre-mRNA 3'-end-processing complex. *EMBO J* **19**: 37–47. doi:10.1093/emboj/19.1.37
- Preker PJ, Lingner J, Minvielle-Sebastia L, Keller W. 1995. The FIP1 gene encodes a component of a yeast pre-mRNA polyadenylation factor that directly interacts with poly(A) polymerase. *Cell* **81**: 379–389. doi:10.1016/0092-8674(95)90391-7
- Rodríguez-Molina JB, O'Reilly FJ, Sheekey E, Maslen S, Skehel JM, Rappsilber J, Passmore LA. 2021. Mpe1 senses the polyadenylation signal in pre-mRNA to control cleavage and polyadenylation. bioRxiv doi:10.1101/2021.09.02.458805
- Russo CJ, Passmore LA. 2014. Electron microscopy: ultrastable gold substrates for electron cryomicroscopy. *Science* **346**: 1377–1380. doi:10.1126/science.1259530
- Schönemann L, Kühn U, Martin G, Schäfer P, Gruber AR, Keller W, Zavolan M, Wahle E. 2014. Reconstitution of CPSF active in polyadenylation: recognition of the polyadenylation signal by WDR33. *Genes Dev* **28**: 2381–2393. doi:10.1101/gad.250985.114
- Schrieck A, Easter AD, Etzold S, Wiederhold K, Lidschreiber M, Cramer P, Passmore LA. 2014. RNA polymerase II termination involves C-terminal-domain tyrosine dephosphorylation by CPF subunit Glc7. *Nat Struct Mol Biol* **21**: 175–179. doi:10.1038/nsmb.2753
- Stowell JAW, Webster MW, Kögel A, Wolf J, Shelley KL, Passmore LA. 2016. Reconstitution of targeted deadenylation by the Ccr4-Not complex and the YTH domain protein Mmi1. *Cell Rep* **17**: 1978–1989. doi:10.1016/j.celrep.2016.10.066
- Sun Y, Zhang Y, Hamilton K, Manley JL, Shi Y, Walz T, Tong L. 2018. Molecular basis for the recognition of the human AAUAAA polyadenylation signal. *Proc Natl Acad Sci U S A* **115**: E1419–E1428. doi:10.1073/pnas.1718723115
- Sun Y, Zhang Y, Aik WS, Yang XC, Marzluff WF, Walz T, Dominiski Z, Tong L. 2020. Structure of an active human histone pre-mRNA 3'-end processing machinery. *Science* **367**: 700–703. doi:10.1126/science.aaz7758
- Takahashi Y, Helmling S, Moore CL. 2003. Functional dissection of the zinc finger and flanking domains of the Yth1 cleavage/polyadenylation factor. *Nucleic Acids Res* **31**: 1744–1752. doi:10.1093/nar/gkg265
- van der Lee R, Buljan M, Lang B, Weatheritt RJ, Daughdrill GW, Dunker AK, Fuxreiter M, Gough J, Gsponer J, Jones DT, et al. 2014. Classification of intrinsically disordered regions and proteins. *Chem Rev* **114**: 6589–6631. doi:10.1021/cr400525m
- Weissmann F, Petzold G, VanderLinden R, Huis In 't Veld PJ, Brown NG, Lampert F, Westermann S, Stark H, Schulman BA, Peters JM. 2016. biGBac enables rapid gene assembly for the expression of large multisubunit protein complexes. *Proc Natl Acad Sci* **113**: E2564–E2569. doi:10.1073/pnas.1604935113
- Wright PE, Dyson HJ. 1999. Intrinsically unstructured proteins: re-assessing the protein structure-function paradigm. *J Mol Biol* **293**: 321–331. doi:10.1006/jmbi.1999.3110
- Young G, Hundt N, Cole D, Fineberg A, Andrecka J, Tyler A, Olerinyova A, Ansari A, Marklund EG, Collier MP, et al. 2018. Quantitative mass imaging of single biological macromolecules. *Science* **360**: 423–427. doi:10.1126/science.aar5839
- Zhang K. 2016. Gctf: real-time CTF determination and correction. *J Struct Biol* **193**: 1–12. doi:10.1016/j.jsb.2015.11.003
- Zhang Y, Sun Y, Shi Y, Walz T, Tong L. 2020. Structural insights into the human Pre-mRNA 3'-end processing machinery. *Mol Cell* **77**: 800–809.e6. doi:10.1016/j.molcel.2019.11.005
- Zhao J, Hyman L, Moore C. 1999. Formation of mRNA 3' ends in eukaryotes: mechanism, regulation, and interrelationships with other steps in mRNA synthesis. *Microbiol Mol Biol Rev* **63**: 405–445. doi:10.1128/MMBR.63.2.405-445.1999